The Role of Normal Fault Growth History in Influencing Fault Seal Potential, Samson Dome, Offshore Norway

A. M. Alghuraybi[1], R. E. Bell[1], and C. A.-L. Jackson[1]

[1]Landscapes and Basins Research Group (LBRG), Department of Earth Science and Engineering, Imperial College London, UK.

Corresponding author: Ahmed Alghuraybi (a.alghuraybi19@imperial.ac.uk)

Key Points:

- Fault growth histories created differences in sealing potential within the studied fault network.
- Samson Dome experienced multiple phases of faulting and doming.
- The driving mechanism behind the development of the Samson Dome remains ambiguous.

Abstract

The growth of normal faults can influence subsurface fluid flow and entrapment within rift basins. However, fault seal studies typically view faults as static structures, with their growth and the potential related temporal changes in hydraulic properties being ignored. In this study, we use borehole data and a high-quality 3D full-stack depth migrated seismic reflection volume to analyse the growth history of the normal fault network in the Samson Dome area, SW Barents Sea. We specifically focus on how the kinematic history of normal faults impacts their sealing properties, whilst also considering their origin and implications for regional salt tectonics. We show that the faults formed during two distinct phases in the Late Triassic and Middle Jurassic-to-Early Cretaceous, and two phases of dome growth occurred in the Late Triassic and Late Cretaceous, challenging existing proposals for the timing of the development of structure. The salt-tectonic origin of the Samson Dome itself remains enigmatic, although mechanical considerations suggest existing models require refinement. Our fault seal analysis reveals a correlation between displacement patterns and sealing potential, as reflected in the Shale Gouge Ratio (SGR) values of different fault groups. More specifically, faults that grew via vertical linkage of initially isolated segments and experienced potential reactivation exhibit lower SGR values, implying a higher likelihood of across and along-fault leakage. Conversely, faults lacking evidence for reactivation or vertical linkage show higher SGR values, suggesting better sealing potential. Notably, the accuracy of our fault seal analysis is greatly influenced by the calculation methods used for V_{shale}, particularly for faults with low displacement. Our study provides valuable insights into the faulting, development, and sealing potential of the Samson Dome area. We also highlight the importance of careful consideration of V_{shale} calculation methods when conducting fault seal analysis.

Plain Language Summary

We examined how normal faults affect fluid movement underground and fluid trapping in the Samson Dome area in the SW Barents Sea. Instead of viewing faults as unchanging, we used borehole data and advanced 3D seismic imaging to study how they grew over time. We focused on how the history of fault movement influences their ability to trap fluids and what this reveals about salt movement. We found that faults formed during two different ancient periods, challenging previous beliefs about their timing. While the origin of Samson Dome is still unclear, our research suggests current explanations might need adjustments. We discovered a link between fault movement and fluid trapping. Faults that connected initially separate segments and might have moved again had weaker trapping abilities, allowing fluids to potentially leak. In contrast, faults that did not show signs of further movement had better trapping abilities, keeping fluids underground more effectively. Overall, our study sheds light on fault growth, fluid trapping, and the importance of accurate value calculations in understanding these processes.

1 Introduction

It is widely accepted that faults can act as barriers to fluid flow by: i) juxtaposing permeable rocks against impermeable rocks (Allan, 1989), or ii) creating an impermeable fault rock that obstructs lateral and vertical migration (e.g., Knipe, 1992; Yielding et al., 1997; Fossen & Bale, 2007; also see review by Manzocchi et al., 2010 and references therein). Alternatively, faults can facilitate fluid flow by acting as high-permeability conduits (Hooper, 1991; Dockrill & Shipton, 2010; Skurtveit et al., 2021). Reservoir simulation models thus need to incorporate faults in a geologically realistic manner (Fisher & Jolley, 2007). Studying the sealing potential of a fault often involves the use of quantitative algorithms that include Clay Smear Potential (CSP) (Bouvier et al. 1989; Fulljames et al. 1997), Shale Smear Factor (SSF) (Lindsay et al., 1993), and/or the most commonly applied method, Shale Gouge Ratio (SGR) (Fristad et al., 1997; Yielding et al., 1997; Freeman et al., 1998). All these methods incorporate some level of analysis of clay content in the faulted sequence (e.g., Freeman et al., 1998; Yielding, 2002; Manzocchi et al., 2010). SGR calculations are influenced by uncertainty in the input parameters, and rely heavily on Vshale calculations, which are susceptible to poorly constrained errors (Bailey et al., 2006). In fact, Bretan et al. (2003) found that a 10% error range can exist in SGR calculations based on how Vshale is estimated. SGR is also not the only factor that influences fault seal capacity, as other factors such as sub-seismic strain (i.e., fractures and deformation bands), fault reactivation, and local variations in fault plane continuity and throw can also impact a fault's sealing potential (Bailey et al., 2006). However, when calibrated using regional data (i.e., dynamic data such as reservoir pressure measurements) and applied consistently, SGR calculations can be used in a relative sense to assess seal potential and capacity across different faults within a given basin (e.g., Yielding, 2002; Bailey et al., 2006; Manzocchi et al., 2010; Yielding, 2015). A key aspect of almost all fault seal studies is that they tend to only consider the present fault geometry, associated juxtapositions, and clay-related hydraulic properties, rarely considering the fault growth history and how seal properties may have changed through time (see Reilly et al., 2017 for an exception). For example, with increasing displacement, SGR and sealing properties might increase. However, the fault may not have been sealing if fluid or gas migration occurred during an earlier phases of fault development, when displacement and related SGR values were lower. Such subtleties would be missed if consider only present-day displacement and juxtaposition relationships.

The Barents Sea is being considered for the long-term geological storage of CO2 (e.g., Riis & Halland, 2014), given it contains many dome-like structures and anticlines (e.g., Mitiku & Bauer, 2013). The Samson Dome is a large, faulted, Mesozoic dome in the SW Barents Sea. Although this structure contains good-quality reservoirs at multiple depths, an exploration well proved that it did not contain hydrocarbons (Norwegian Petroleum Directorate, 2023), making it a possible candidate for future CO2 storage projects. However, the SW Barents Sea has a well-documented history of fault-related fluid leakage related to post-trap filling regional uplift (e.g., Makurat et al., 1992; Doré & Jensen, 1996; Gabrielsen et al., 1997; Ostanin et al. 2013; Vadakkepuliyambatta et al., 2013; Hermanrud et al., 2014; Mohammedyasin et al., 2016; Edmundson et al., 2020; Argentino et al., 2021). It is therefore vital to undertake a detailed assessment of the hydraulic properties of the fault network above the Samson Dome, with explicit recognition of its complex geometry and kinematic history.

The Samson Dome is a structural high on the Bjarmeland Platform, located between the Hammerfest and Nordkapp basins (e.g., Gabrielsen et al., 1990; Breivik et al., 1995). The few studies that have focused on the Samson Dome examined it at a regional scale using 2D seismic reflection (e.g., Gabrielsen et al., 1990; Vadakkepuliyambatta et al., 2013) and gravity data (e.g., Breivik et al., 1995), interpreting it as a salt-related (i.e., inflated) anticline (e.g., Gabrielsen et al., 1990; Breivik et al., 1995; Mattos et al., 2016). Mattos et al. (2016) use regional 2D and 3D pre-stack time migrated seismic reflection and borehole data to investigate the salt-related structural evolution of the Samson Dome by analysing the geometry and kinematics of the related normal fault networks, suggesting doming and the main stage of faulting happened in the Late Cretaceous, coincident, and therefore driven by, opening of the North Atlantic Ocean. In this study, we use borehole data and a high-quality 3D full-stack depth seismic reflection volume that was generated using a Full-Waveform inversion velocity model (Jones et al., 2013) to study the growth history of the normal fault network in the Samson Dome area. Whereas Mattos et al. (2016) focus on using fault geometries and kinematics to understand the halokinetic history of the Samson Dome structure, we concentrate here on examining how the kinematic history and normal fault growth patterns might have influenced the faults' sealing potential and propose an alternative model for the development of the Samson Dome and its related fault network. A subsequent study by Alghuraybi et al. (2023b) provides a quantitative analysis of the velocity differences within the fault zones of the fault network studied here and tests possible links between fault zone velocity variations to the faults' kinematic history and fault seal potential.

2 Geological Setting

The Barents Sea is located in the northwest corner of the Eurasian tectonic plate south of the Arctic Ocean (Figure 1) (e.g., Gabrielsen, 1984; Doré, 1995). The SW Barents Sea developed in response to multiple phases of crustal extension, which formed predominately NNE-trending rift basins (e.g., Nordkapp Basin, Hammerfest Basin) and basement highs (e.g., Loppa High, Norsel High; Figures 1 and 2) (e.g., Faleide et al., 1984; 2008; 2015; Gabrielsen, 1984; Gabrielsen et al., 2016). The oldest rocks in the SW Barents Sea are Late Cambrian to mid-Devonian (i.e., Caledonian) igneous and metamorphic rocks, which contain fabrics and structures that influenced the evolution and present structural framework of the area (e.g., Faleide et al., 1984; Ritzmann & Faleide, 2007). The collapse of the Caledonian orogenic belt in the Devonian marked the onset of the first rift phase, which lasted until the Carboniferous (e.g., Faleide et al., 2008). Late Devonian to Carboniferous rifting created narrow basins that were initially filled during the latest

Carboniferous to Permian by evaporites and carbonates, followed by siliciclastic rocks (e.g., Faleide et al., 1984). Significant accommodation was created during the second, Late Permian rifting phase, which was subsequently infilled by further clastic sedimentation that continued into the Triassic (e.g. Johansen et al., 1993; Larssen et al., 2002; Glørstad-Clark et al., 2010; Harishidayat et al., 2015). The third rifting phase occurred during the Middle Jurassic – Early Cretaceous and led to the formation of large, widespread basins between structural highs (e.g. Gabrielsen, 1984; Faleide et al., 1993; Doré, 1995; Faleide et al., 2008). Following the third rifting phase, clastic sedimentation continued during the Late Cretaceous, with a major regional unconformity forming at the base of the Paleogene in response to regional uplift (e.g., Faleide et al., 2008). The opening of the Norwegian and Greenland seas during the Palaeocene – Eocene is thought to be linked to the fourth rifting phase in the SW Barents Sea (e.g., Eldholm & Thiede, 1980; Faleide et al., 2008; Harishidayat et al., 2015).

Numerous salt diapirs have been described in the SW Barents Sea, in areas close to the Samson Dome (e.g., the Nordkapp Basin; Nilsen et al., 1995; Rojo et al., 2016; Paoletti et al., 2020). However, the geometries and seismic expression of these structures and adjacent depocentres (i.e., narrow, km-tall, seismic chaotic diapirs, flanked by seismically reflective minibasins) in the Nordkapp Basin are clearly different from those characterising the Samson Dome (see below). Thick (c. 2 – 4 km), evaporite-dominated layers were deposited across the Barents Sea shelf following the Late Carboniferous – Early Permian rift phase (e.g., Nilsen et al., 1995; Gudlaugsson et al. 1998). More recent work estimates the average (depositional) salt thickness within the Nordkapp Basin was c. 2.5 km (e.g., Grimstad, 2016). A combination of sediment loading (e.g., Grimstad, 2016; Rowan & Lindsø, 2017) and thick-skinned extension (i.e., basement-involved normal faulting; e.g., Jensen & Sørensen, 1992; Nilsen et al., 1995) drove salt mobilisation within the Nordkapp Basin.

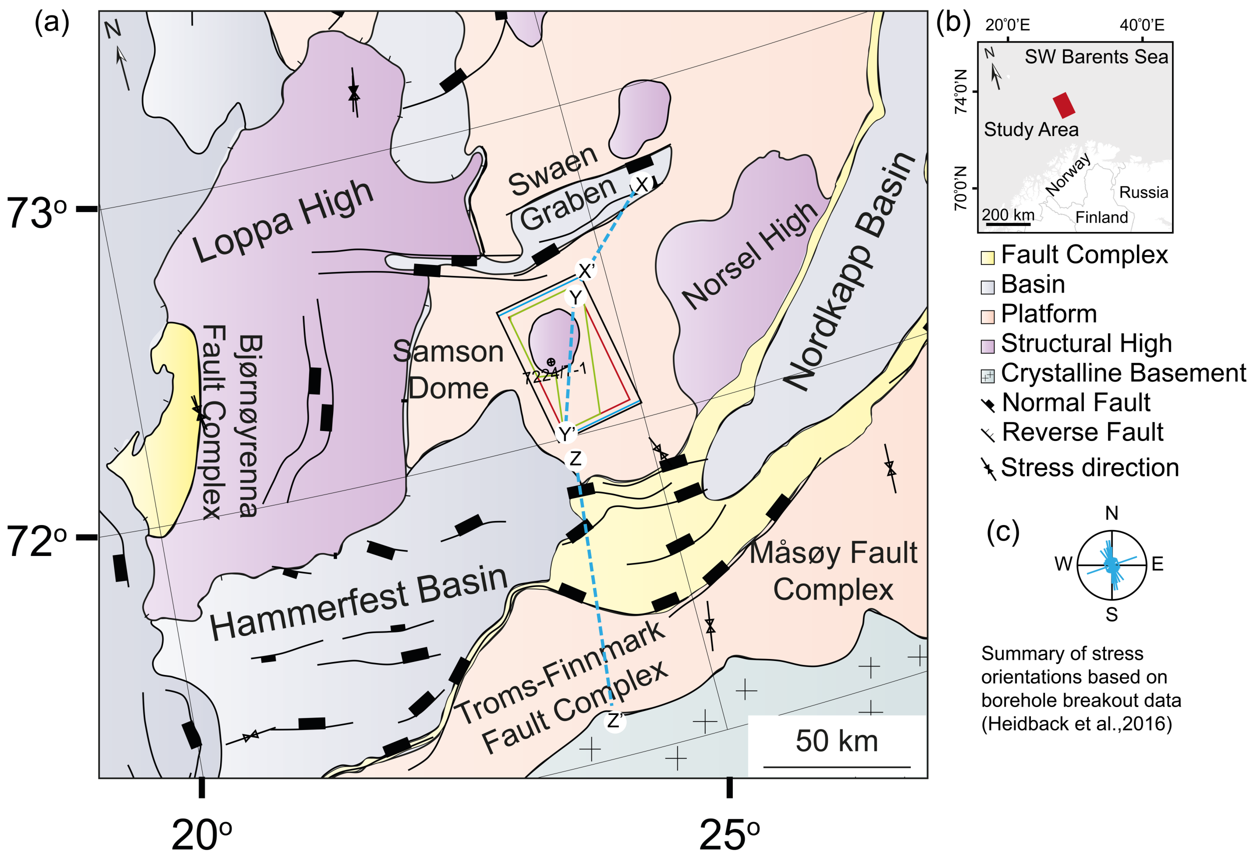

Figure 1. (a) A map summarising the regional structural elements of the SW Barents Sea around the Samson Dome structure. The dashed lines denoted with X, X', Y, Y', Z, Z' are indicating the location of the regional seismic lines in Fig. 2. The map is modified after information found in the Norwegian Petroleum Directorate fact page http://www.npd.no/en/. **(b)** A subset location map highlighting the geographical location of the study area. **(c)** A summary of the present-day maximum horizontal stress orientations based on borehole breakout data retrieved from the World Stress Map (Heidback et al., 2016).

The current model for the structural evolution of the Samson Dome suggests the main phase of salt mobilisation was somehow triggered by extension caused by the opening of the North Atlantic Ocean in the Early to Late Cretaceous. This is based on the observation that Late Cretaceous strata are folded into a broad dome (e.g., Mattos et al., 2016). The proposed thickness of salt required to inflate a structure the size of the Samson Dome is substantial (3.5 km; e.g., Gabrielsen et al., 1990; Breivik et al., 1995). Consequently, we would expect to observe structures related to complimentary salt withdrawal, e.g., minibasins, supra-salt faulting, welds (e.g., Jackson & Talbot, 1986; Nilsen et al., 1995; Koyi, 1998; Jackson & Hudec, 2005; Hudec & Jackson, 2007; Pichel et al., 2018; Rojo et al., 2019). Although such salt-related structures have been documented regionally (i.e., in the Nordkapp Basin; e.g., Rojo et al., 2019), and despite supra-salt faulting being locally intense above and around the Samson Dome (Mattos et al., 2016), they are notably absent from the Samson Dome area (Figure 2). Seismic reflection data also show that the Samson Dome is not underlain by the characteristic, chaotic, variable amplitude seismic facies that defines salt structures in the Nordkapp Basin (e.g., Hassaan et al., 2021) and other salt-bearing sedimentary basins (e.g., Jackson and Hudec, 2017) (Figure 2). This calls into question the interpretation of the Samson Dome as a salt-tectonic structure purely related to halokinesis (i.e., salt flow induced purely by gravity; Jackson and Hudec, 2017).

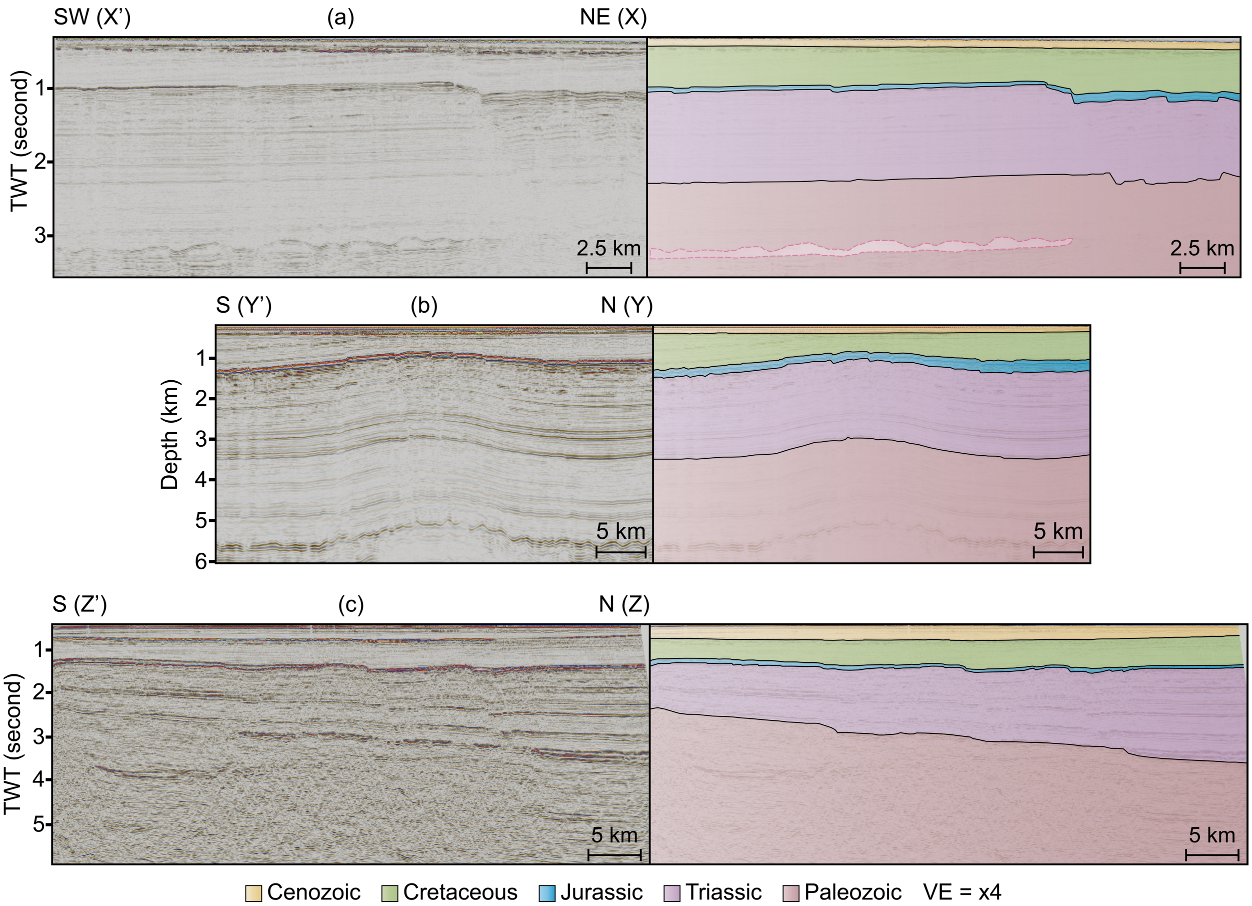

Figure 2. Un-interpreted (left) and interpreted (right) regional seismic sections showing the overall structural style and stratigraphy around the Samson Dome **(b)**. The section north of the Samson Dome **(a)** shows features that might relate to carbonate build-ups or salt bodies. Similar features are not observed on the other two section.

3 Data and Methods

We used the BG1002 3D seismic reflection volume, which was acquired by CGG in 2010 and reprocessed by BG Geophysical Operations in 2013. We retrieved the data from the DISKOS database (https://portal.diskos.cgg.com/whereoil-data/). The 3D survey covers an area of c. 1100 km^2 and is a full-stack depth migrated (PSDM) volume that was generated using a Full-Waveform inversion (FWI) velocity model (Jones et al., 2013). The survey in-lines trend NNW, whereas the cross-lines trend ENE. The survey was acquired with 10 streamer arrays, each with 480 groups and a 6 km cable length. The shot and group intervals were 25 m and 12.5 m, respectively. The total recording time was 5050 ms two-way time, and the data were processed with a 4 ms sampling interval and a zero-phase wavelet. We displayed the data using the reverse SEG polarity convention, where a downward increase in acoustic impedance is represented by a trough (coloured blue) and a decrease by a peak (coloured red). The seismic resolution ranges from approximately 10 m to 70 m from depths of 500 to 3500 km, an estimate based on half the seismic wavelength of the PSDM volume. A full processing report can be accessed from the DISKOS database (https://portal.diskos.cgg.com/whereoil-data/) by searching for "BG1002 3D." The final PSDM volume generated using the FWI velocity model runs from 0 m to 6000 m and is sampled every 10 m (Jones et al., 2013). We also used data from wellbore 7224/7-1 that drilled a total depth of c. 3100 m. This wellbore provided age and lithological constraints down to Early Triassic (Olenekian) strata (https://factpages.npd.no/en/wellbore/PageView/Exploration/All/1245).

Our seismic interpretation included horizon and fault mapping, and seismic attribute analysis (see below) that was performed using industry standard software. We interpreted a total of 16 horizons throughout the PSDM volume, the ages of which were constrained by well-log and biostratigraphic data from wellbore 7224/7-1 (Figure 3). We initially used a systematic grid interpretation with 32-line spacing (375 m), which we later used as an input for 3D auto-tracking.

In areas where 3D auto-tracking was not possible or did not perform well due to poor data quality, we conducted manual interpretation every line (12.5 m). We used the interpreted horizons in the geometric and kinematic analysis of the fault network. We also used seismic attributes, namely variance, which helps to reveal the geometry of the fault network by highlighting discontinuities in the seismic signal (Figure 4; e.g., Randen et al., 2001).

The 3D nature of the PSDM volume allowed us to conduct a quantitative analysis of the fault structure and displacement using arbitrary seismic lines oriented normal to local strike (e.g., displacement-length (T-x) plots; e.g., Cartwright et al., 1995; Jackson et al., 2017). We also produced depth-structure and thickness maps to analyse (plan-view) fault geometries and kinematics, respectively (e.g., Childs et al., 2003; Jackson & Rotevatn, 2013; Childs et al., 2017; Jackson et al., 2017). We also created (displacement) strike-projections (e.g., Walsh and Watterson, 1991 and Alghuraybi et al., 2022) and calculated fault aspect ratios (i.e., fault trace length divided by fault maximum height, e.g., Nicol et al., 1996; Alghuraybi et al., 2023a). These various methods helped us describe the geometry and growth history of the fault network (see review by Jackson et al., 2017).

Finally, we calculated SGR for each fault to investigate any potential relationships between fault geometry, growth history, and sealing properties (as expressed by SGR). To constrain the clay content of the host sequence we used data from wellbore 7224/7-1, including Gamma Ray (GR) well-log data and lithology descriptions from cuttings. However, we did not have access to a volume of shale (V_{shale}) log or any dynamic data to QC or calibrate our calculated SGR results. We therefore estimated the V_{shale} from GR log data using two approaches. We first calculated a linear V_{shale} (see Appendix 1, Eq. 1) and secondly, we calculated a non-linear V_{shale} log using the Clavier et al. (1971) equation (Appendix 1, Eq. 2). These equations only approximate the actual formation V_{shale} as it is derived from GR data, which can be affected by the presence of radioactive minerals, matrix density, and clay type (e.g., Clavier et al., 1971). Therefore, any derived properties used here based on the V_{shale} calculations (i.e., SGR) should only be taken as an approximation of the fault/rock property and not an exact measurement. There is significant uncertainty in our fault seal analysis that arises from the limited wellbore control in the area. In detail, the fact that we have only one wellbore that provided age and lithology control means that we are not accounting for any lateral facies or lithological changes across stratigraphic intervals. We generated SGR strike-projections (similar to the displacement strike-projections mentioned above) to analyse the 3D distribution of SGR values across fault planes. Additionally, we plotted SGR values along the length of the fault across key stratigraphic levels to highlight any variability in fault seal potential along the fault. Lastly, we used displacement backstripping to calculate SGR through time and note any changes in fault seal potential through time (see review by Jackson et al. 2017).

Figure 3. Stratigraphic column for SW Barents Sea showing major tectonic events. The figure shows the major seismic horizons picked in the area and near the well location.

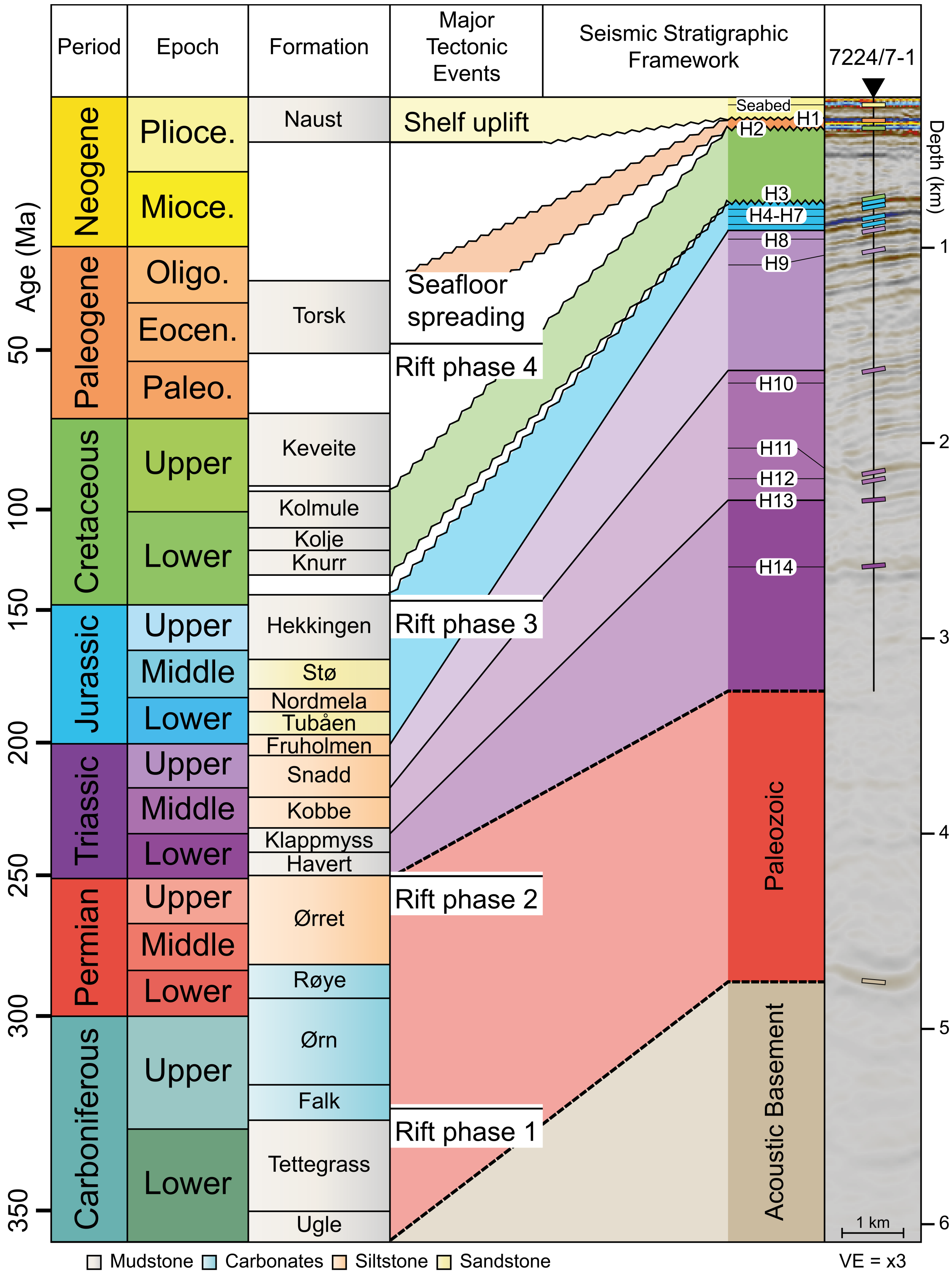
Period
Epoch
Formation
Major Tectonic Events
Seismic Stratigraphic Framework
7224/7-1
Age (Ma)
50
100
150
200
250
300
350
Neogene
Paleogene
Cretaceous
Jurassic
Triassic
Permian
Carboniferous
Plioce.
Mioce.
Oligo.
Eocen.
Paleo.
Upper
Lower
Upper
Middle
Lower
Upper
Middle
Lower
Upper
Middle
Lower
Upper
Lower
Naust
Torsk
Keveite
Kolmule
Kolje
Knurr
Hekkingen
Stø
Nordmela
Tubåen
Fruholmen
Snadd
Kobbe
Klappmyss
Havert
Ørret
Røye
Ørn
Falk
Tettegrass
Ugle
Shelf uplift
Seafloor spreading
Rift phase 4
Rift phase 3
Rift phase 2
Rift phase 1
Seabed
H1
H2
H3
H4-H7
H8
H9
H10
H11
H12
H13
H14
Paleozoic
Acoustic Basement
Depth (km)
1
2
3
4
5
6
1 km
Mudstone
Carbonates
Siltstone
Sandstone
VE = x3

252
253

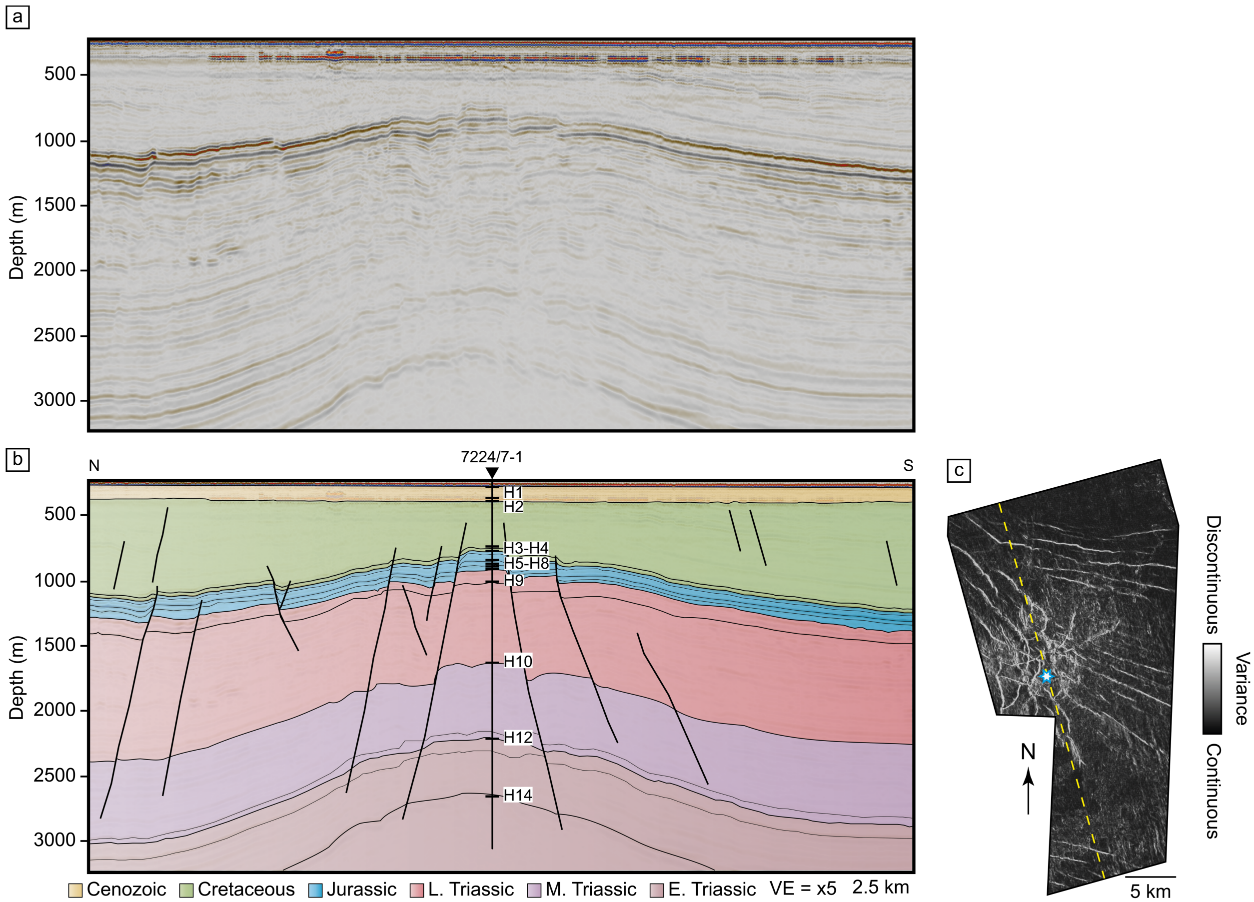

Figure 4. A representative seismic section illustrating the structural and stratigraphic elements in the study area. **(a)** Un-interpreted section. **(b)** Interpreted section including the location and extent of wellbore 7224/7-1. **(c)** a variance slice along the H3 horizon highlighting the fault network as seismic discontinuities in white. The seismic section is indicated by the yellow dashed line and the blue and white star shows the location of the wellbore.

4 Results

4.1 Strucutral elements

The Samson Dome is elliptical in map view, with a N-trending major radius of c. 13 km and an E-trending minor radius of c. 9 km (Figure 5) The folding appears prominent across all strata between the Lower Cretaceous and the acoustic basement (Figure 4). Despite the poor seismic quality at depths >2 km, below the main, seismically well-imaged part of the dome, we do not see an obvious salt body (Figure 2). Instead, we observed moderately reflective, mounded bodies that may be the seismic expression of Late Carboniferous to Early Permian carbonate mounds (Figures 2 and 3) (e.g., Ahlborn et al., 2014; Di Lucia et al., 2017; Elvebakk et al., 2002). The interpretation of carbonate mounds is consistent with regional observations in the SW Barents Sea and is constraint by seismic reflection and wellbore data regionally (e.g., Larssen et al., 2002; Rafaelsen et al., 2008; Di Lucia et al., 2017; Hassaan et al., 2020). The top of the Samson Dome exhibits radial faulting, whereas the study area generally appears to be dominated by NW-striking and EW- to WNW-striking faults (Figures 4 and 5). In detail, we mapped 48 faults and identified four main groups of normal faults.

The first fault group is restricted to the Cretaceous interval (Figures 6. a. i and 7. a, b) and is largely restricted to the dome flanks (Figure 6. a. i). The displacement on these faults is typically <50 m, with individual faults being 0.5-4 km long (Figure 7. a, b). South of the Samson Dome, the faults exhibit a more consistent strike direction of E-W to ESE-WNW and generally dip southward, whereas north of the structure they are more polygonal (i.e., they show no preferred strike or dip direction; Figures 6. a. i and 7. a, b).

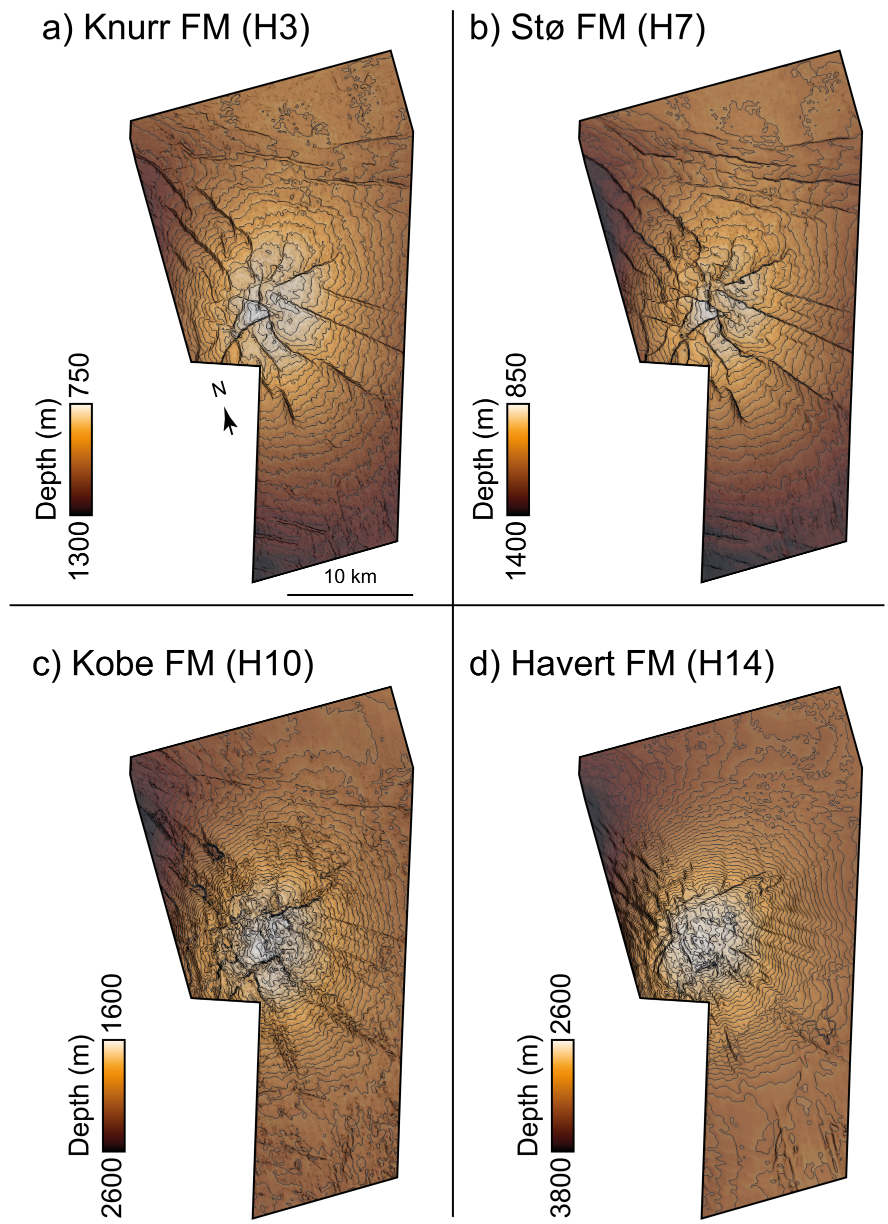

Figure 5. Depth structure maps for horizons H3 **(a)**, H7 **(b)**, H10 **(c)** and H14 **(d)**.

The second fault group includes 11 faults that offset Upper Triassic to Lower Cretaceous stratigraphy (Figures 6. a. ii, b and 7. b, c). Six faults (F1, F37, F40, F42, F46, and F48). In contrast to the first fault group, these faults are restricted to the NE of the study area, on the crest of the dome. Like the first group, however, they also strike ESE-WNW, but are shorter (<500 m long) and have lower displacements (c. 10 m in the lowermost Cretaceous). The other five faults (F3, F4, F6, F7, and F32) are longer (maximum lengths of c. 8 km) and have higher displacements (c. 50 m). (Figures 6. a. ii, b and 7. b, c).

The third fault group consists of 17 faults that offset Middle Triassic to Early Cretaceous stratigraphy, which we sub-divided into two subgroups. The first subgroup includes two WNW-striking faults (F2 and F5) located on the NE flank the dome. They have a maximum length and displacement of c. 7 km and c. 80 m, respectively (Figures 6. a. ii, b and 7. b, d). The other two faults (F25 and F26) are found on the SW side of the study area towards the flank of the dome, and show a maximum trace length and displacement of c. 6 km and c. 45 m, respectively (Figures 6. a. ii, b and 7. e). The second subgroup comprises 13 predominately NW-SE-striking faults that occur on the dome crest (F13, F18, F19, F29, F33, F43, and F44) and flanks (F8, F14, F15, F41, F45, and F47) (Figure 6. a. ii, b). These faults are 0.5-5.5 km long and have displacements of <10-85 m (Figure 7. a, e, f, g).

The fourth and final fault group is composed of 20 faults that offset Lower Triassic to Lower Cretaceous stratigraphy. These faults strike mainly NW-SE and occur on the NW and SE flanks of the dome (F9, F12, F16, F21, F22, F23, F24, F28, F39) or on the dome apex (F10, F11, F17, F20, F27, F30, F31, F34, F35, F36, F38) (Figure 6. a. ii, b). These faults have variable trace lengths (0.35-12 km), with an average trace length of c. 4 km, and an average maximum displacement of c. 55 m (ranging from c. 5-90 m) (Figure 7).

An alternative way to classify the fault network is to separate the faults according to their strike, dip, and dip direction. By plotting these parameters on a stereonet and rose diagram, we can subdivide the fault network into four subsets (Figure 6. c. i, ii). These four subsets generally correlate well with the fault grouping described above. For instance, subsets 1 and 3 broadly correlate to the second and third fault groups, whereas subsets 2 and 4 capture faults that are part of the fourth fault group. The fourth fault group includes faults that show evidence of growth by vertical linkage (see below) and strikes that are parallel to the present-day maximum horizontal stress direction based on borehole breakout data (Heidbach et al., 2016) (Figure 6. c. iii).

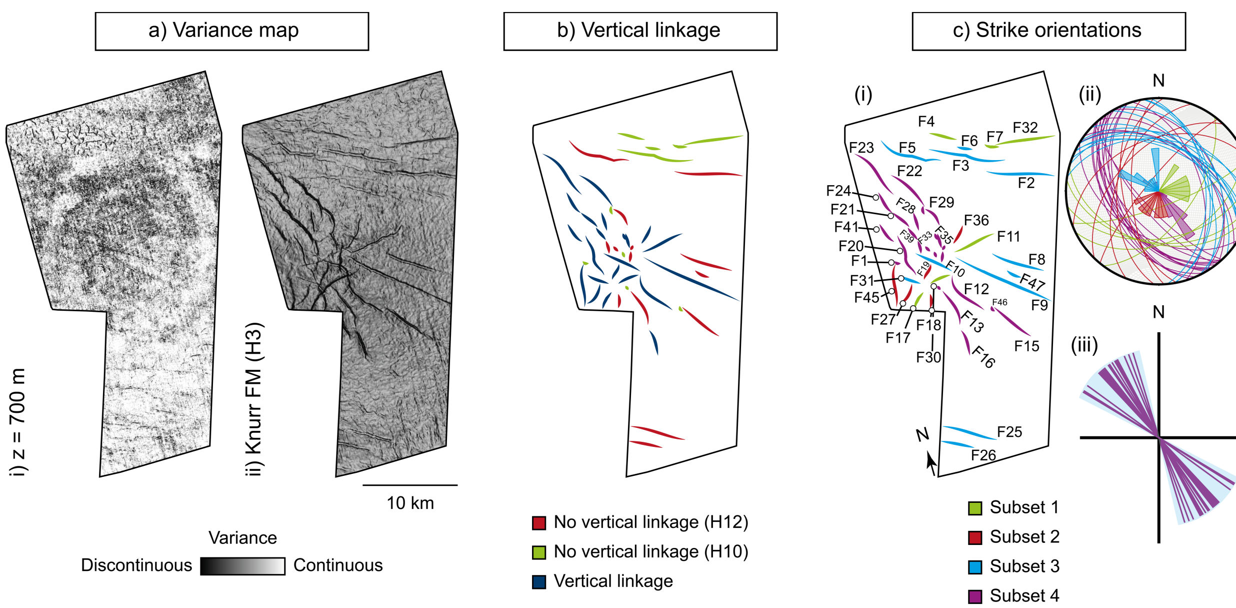

Figure 6. (a) A variance map taken at a depth of 700 m **(i)** and along the top of Knurr FM – H3 **(ii)**. These two variance slices illustrate the different faulting styles with depth where the shallow slice (i) shows evidence of polygonal faulting in the north to northwest while (ii) highlights the predominance of the NW-trending faulting. **(b)** Th spatial distribution of the studied fault network colour-coded by evidence of vertical linkage (dark blue), no evidence of vertical linkage with base fault tip along H10 (green) and H12 (red). **(c)** The spatial distribution of the studied fault network colour-coded by strike orientations **(i)** and stereonet and rose diagram with the colours corresponding to the ones shown on the map **(ii)**. **(iii)** strike-orientations of the faults trending NW (purple lines) and the light blue shading shows the direction of the present-day maximum horizontal stress.

Figure 7. Eight seismic sections taken perpendicular to strike of different fault within the network. The locations of the seismic sections are shown on the accompanying variance map of H3. These seismic sections try to capture the faulting styles and geometries of the studied fault network.

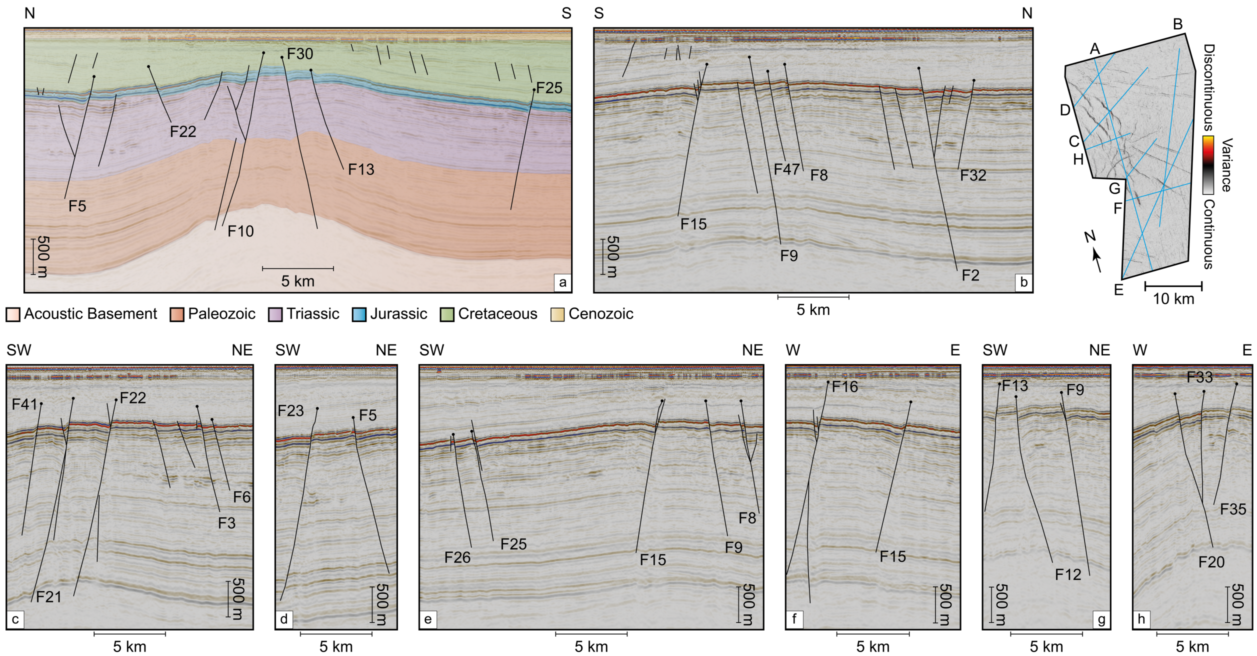

4.2 Fault network geometry

By closely examining the geometry of the fault network, we note that the studied faults lack any clear along-strike bends (Figure 6. a) and are generally planar (Figure 7). Nearly all the studied faults (n=44) have their maximum displacement across the Lower Cretaceous to Lower Jurassic intervals (H3 and H7) and show broad, bell-shaped displacement-length profiles (Figure 8. a. i, ii). These faults are similar to a suite of faults studied by Alghuraybi et al. (2023a) over the Troms-Finnmark Fault Complex. However, we note some internal variability within the Samson Dome fault network, with evidence of displacement partitioning between faults as shown by multiple displacement maxima and local minima across the same stratigraphic level (e.g., F21 in Figure 8. a. i). These multiple displacement maxima could indicate that the faults grew via the linkage of smaller, previously isolated segments (e.g., Cartwright et al., 1995; Childs et al., 2003).

The variable nature of the displacement is most clearly seen across the H10 (i.e., Middle Triassic) stratigraphic interval (Figure 8. a. iii). For example, some faults show bi-modal displacement patterns along H10 (that is, two displacement maxima separated by a displacement minimum; see F9, F11 and F25 in Figure 8. a. iii). In contrast, other faults (i.e., F2, F12, F16, F21, F23, and F35) generally show broad, bell-shaped displacement-length patterns for H10 (Figure 8. a. iii).

Displacement across the H14 stratigraphic level (i.e., Lower Triassic) is only present on faults with multiple displacement maxima along different stratigraphic intervals separated by a displacement minimum (i.e., the fourth fault group; Figure 9.b). We infer these faults to have experienced growth via vertical linkage (e.g., Nicol et al., 1996). The displacement-length patterns for these faults across H14 are also variable, being similar to the patterns described across H10 (Figure 8. a. iv). However, in terms of their maximum displacement (D_{max}) and length (L_{max}), regardless of the structural level of observation (i.e., H10 or H14), the fault network plots within the scatter of a global dataset of normal faults (Lathrop et al., 2022) (Figure 8. c). The network shows a D_{max}/L_{max} scaling relationship between 0.1 and 0.001 (Figure 8. c). Additionally, all faults have an aspect ratio <5, with a mean ratio of 1.6 for the 48 faults we studied in detail (Figure 8. d).

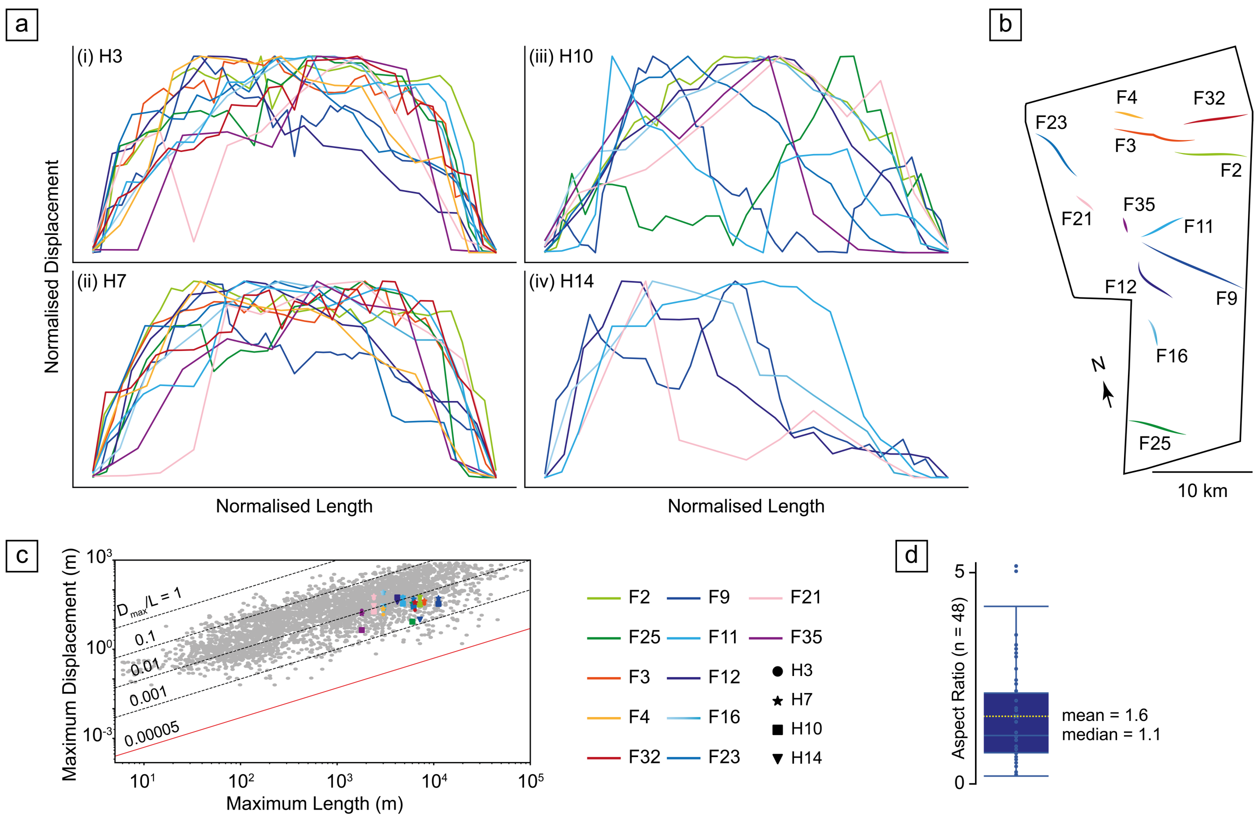

Figure 8. A summary of the geometric properties of 12 fault examples representing the fault network. (a) Normalised displacement-length for (i) the Early Cretaceous top Knurr FM (H3), (ii) the Early-Middle Jurassic Stø FM (H7), (iii) the Middle Triassic Kobbe FM, and (iv) the Early Triassic Havert FM (H14). (b) Spatial distribution of the selected faults across the study area with each fault highlighted with a different colour. (c) D_{max}-L_{max} plot from a global database of normal faults (modified after Lathrop et al., 2022). (d) A box plot of the aspect ratio values for the studied fault network. The fault network has typical aspect ratio values of natural normal faults with a maximum aspect ratio of 5 and a mean of 1.6.

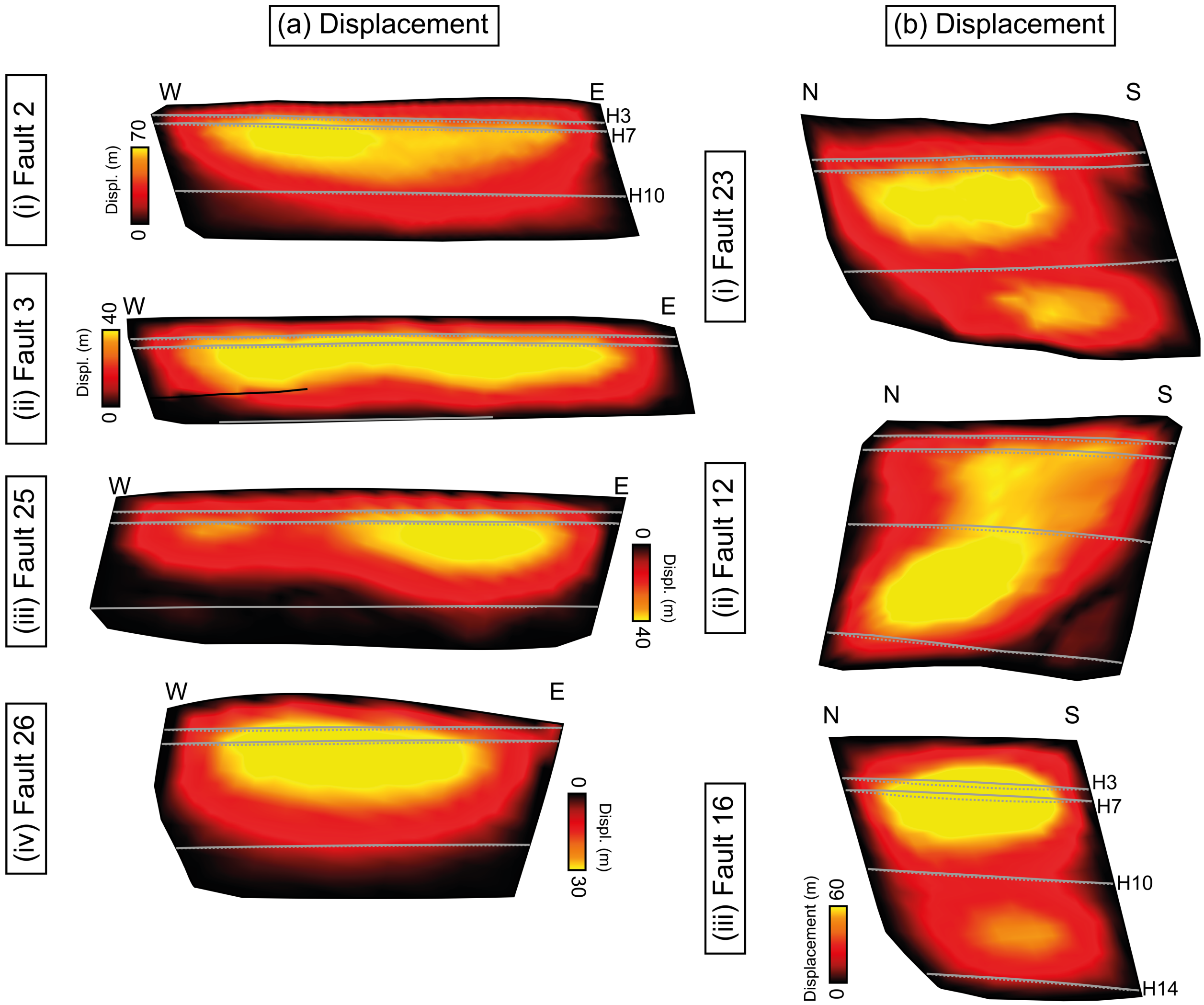

Figure 9. Strike-projected displacement distribution along the fault surface. The four fault examples shown in **(a)** Fault 2 **(a.i)**, Fault 3 **(a.ii)**, Fault 25 **(a.iii)**, and Fault 26 **(a.iv)** represent faults in subset 3. The three fault examples shown in **(b)** Fault 23 **(b.i)**, Fault 12 **(b.ii)**, and Fault 16 **(b.iii)** are part of fault subset 4. Three key horizons (H3, H7, and H10) are indicated by light grey lines on the strike-projections (a) & (b).

4.3 Fault network kinematics

4.3.1 Observations

Our detailed mapping shows that during the Paleozoic, deposition was regionally isopachous, with local thinning across the top of what we interpret as carbonate mounds (Figure 10. a). The regionally isopachous deposition appears to have continued during the Early and Middle Triassic, with minor, highly localised, across-fault thickening (c. 200 – 250 m) around the crest of the dome along NW-SE-striking faults (Figure 10. b). In contrast, the overlying Upper Triassic interval thins towards the dome apex (Figure 10. c. i). The thickness difference between the dome crest and distal flanks is up to 600 m. Whilst this regional, dome-related thickness pattern is most apparent within the Snadd Formation (Figure 10. c. ii-iii), it also occurs in the overlying Fruholmen Formation, which also shows more localised, across-fault thickening (c. 100 – 150 m) associated with NW-SE-striking structures (Figure 10. d). Note that we do not observe any clear thickness variations across or along other faults within the network (i.e., those not striking NW-SE) (Figure 10. b – d).

In contrast to Triassic strata, whose thickness is primarily related to the Samson Dome and during the latter stages, NW-SE faulting, deposition during the Jurassic appears to be controlled only by faulting, with notable across-fault thickening (c. 100 – 200 m) along most faults within the studied fault network and isopachous deposition elsewhere (Figure 11. a). Fault-controlled deposition likely continued into the Early Cretaceous during deposition of the Knurr Formation, which also shows regional isopachous deposition with minor across-fault thickening (up to c. 90 m) in association most of the faults within the network (Figure 11. b). The Late Cretaceous marked a shift in deposition from across-fault thickening to regional isopachous deposition with significant thinning (c. 500 m) towards the crest of the dome (Figure 11. c). The Cenozoic thickness map reveals largely isopachous deposition with local evidence of erosion (Figure 11. d).

4.3.2 Summary and interpretation

In summary, the overall structure of the Samson Dome developed over multiple phases following deposition of Late Carboniferous to Early Permian carbonate mounds. First, some of the NW-SE-striking faults initiated during the Early to Middle Triassic, as is evident by the development of depocenters along segments of these faults (Figures 10. B and 12. b). However, most of the faults within the fault network developed during the Middle Jurassic to Early Cretaceous, with faults that initiated earlier, in the Triassic, remaining active (Figures 10. d; 11. a-b and 12. c-f). The cessation of across-fault thickening and the position of the fault upper tips indicate that faulting stopped during the Late Cretaceous (Figure 11. b; see also Appendix 2 for backstripped displacement vs. length profiles).

In contrast to faulting, which commenced in the Early to Middle Triassic, growth of the Samson Dome appears to have initiated in the Late Triassic, during the deposition of the Snadd Formation (Figures 10. C and 12. c). We do not observe any evidence of doming during the Jurassic and Early Cretaceous (Figures 11. a-b and 12. e, f), although thinning and onlap of age-related strata towards the dome suggest resurgence of the dome during the Late Cretaceous, after a period of quiescence (Figures 11. C and 12. g). Therefore, by combining all of the observations presented above, we propose that the structures at the Samson Dome area developed through two phases of faulting in the Late Triassic and Middle Jurassic – Early Cretaceous and two phases of doming that occurred during the Late Triassic and Late Cretaceous. No clear faulting or dome growth occurred during the Cenozoic (Figure 12. h).

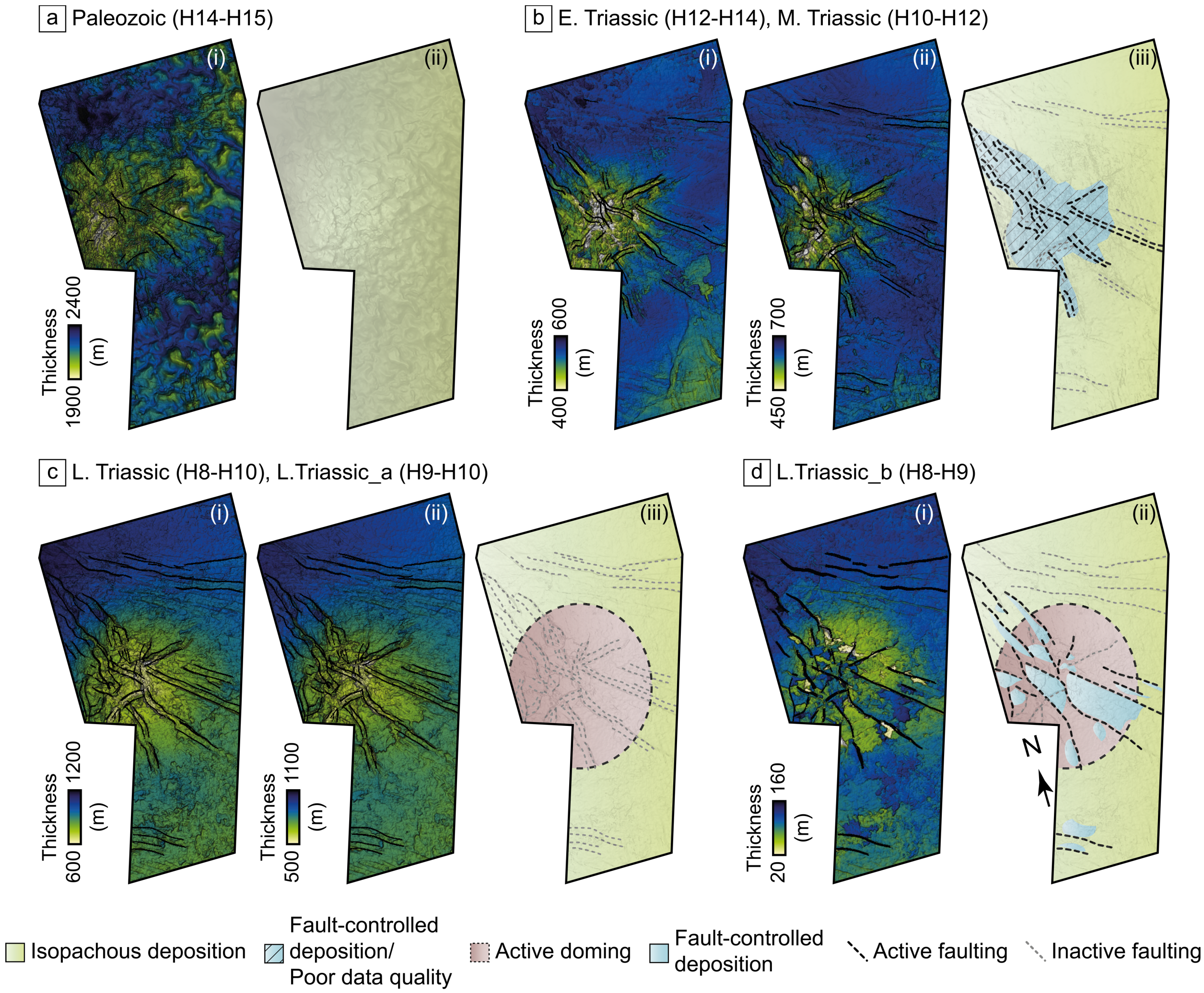

Figure 10. Isopach (thickness) maps for the Paleozoic interval between the interpreted acoustic basement (H15) and the top Havert FM (H14) **(a)**, Early Triassic interval between the Havert (H14) and Klappmyss FM (H12) **(b.i)**, Middle Triassic interval between Klappmyss FM (H12) and Kobbe FM (H10) **(b.ii),** Late Triassic interval between Kobbe FM (H10) and Fruholmen FM (H8) **(c.i)**. The Late Triassic interval is divided into two sections a lower interval between Kobbe FM (H10) and Snadd FM (H9) and an upper interval between Snadd FM (H9) and Fruholmen FM (H8). A schematic interpretation of each interval is shown in **(a.ii)**, **(a.iii)**, **(c.iii)** and **(d.ii)**. These isopachs show temporal variations in depositional styles across these time intervals.

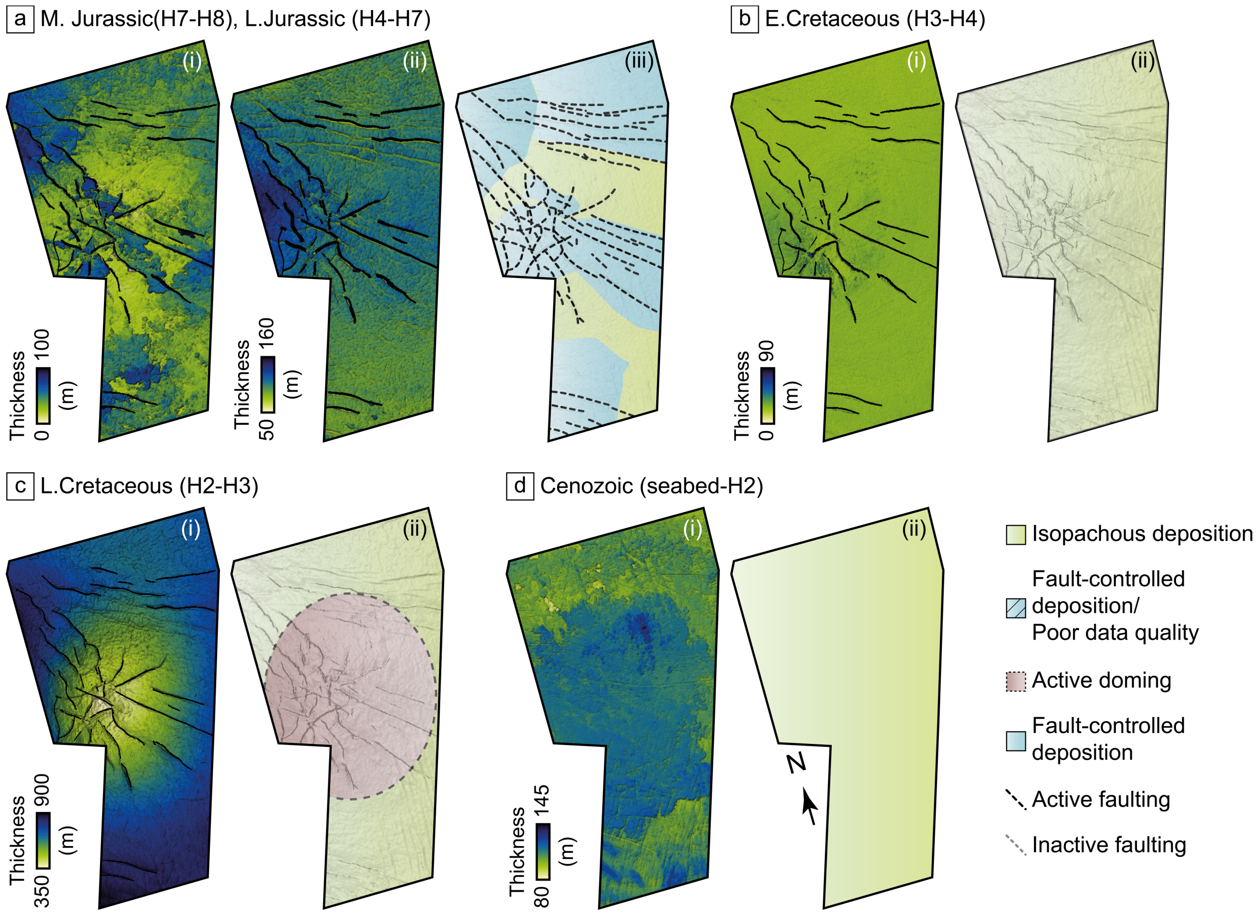

Figure 11. Isopach (thickness) maps for the Middle Jurassic interval between Top Fruholmen FM (H8) and Top Stø FM (H7) **(a.i)**, Late Jurassic interval between Top Stø FM (H7) and Top Hekkingen FM (H4) **(a.ii)**, Early Cretaceous interval between Top Hekkingen FM (H4) and Top Knurr FM (H3) **(b.i)**, Late Cretaceous interval between Top Knurr FM (H3) and Top Kolmule FM (H2) **(c.i)**, and the Cenozoic interval between Top Kolmule FM (H2) and present-day seabed surface (seabed) **(D.i)**. A schematic interpretation of each interval is shown in **(a.iii)**, **(b.ii)**, **(c.ii)** and **(d.ii)**. These isopachs show temporal variations in depositional styles across these time intervals.

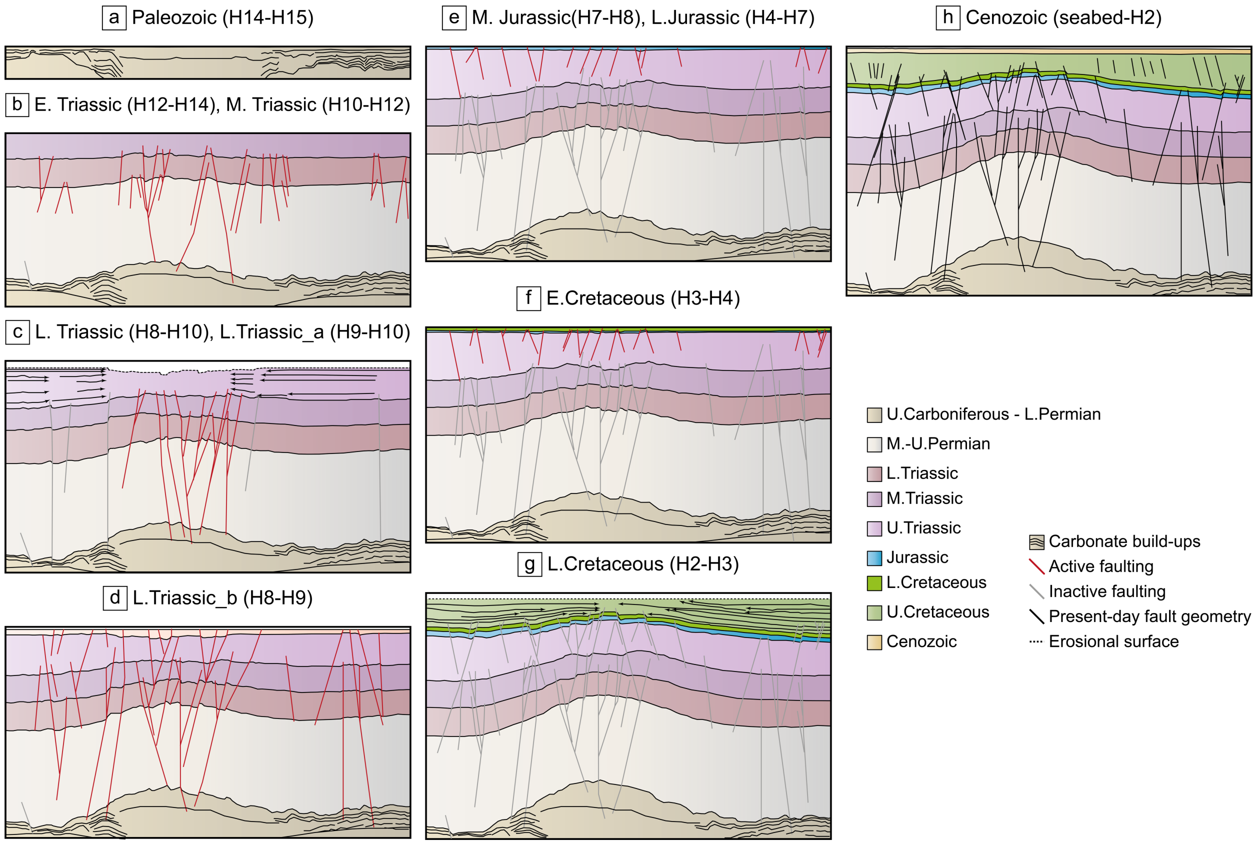

Figure 12. A proposed structural evolution model of the Samson Dome. The model includes **(a)** carbonates build-up, **(b)** first phase of faulting, **(c)** first phase of doming, **(d)** second phase of faulting, **(e)** third phase of faulting, **(f)** second phase of doming and **(g)** isopachous deposition.

4.4 Fault seal analysis

Having documented the geometry and kinematic evolution of the Samson Dome and related fault network, we calculated SGR values for the latter using their present-day displacement and V_{shale} values estimated from GR logs in wellbore 7224/7-1 (see methods). We then used strike-projections to visualise 3D variations in SGR across the fault surface. Therefore, the only factors that influence our SGR calculations are displacement variations within the fault network and any seismically defined changes in stratal thickness. However, in this study we focus on potential long-term (i.e., geological timescale) changes in fault seal caused by fault growth history and not relatively shorter-term (i.e., production timescale) changes in the probability of cross-fault flow.

We used seven examples to demonstrate the potential impact of fault growth history on temporal changes in sealing characteristics and likelihood. These seven examples were divided into two groups. The first group includes four faults that show a single displacement maximum and do not display any evidence of growth via vertical linkage (F2, F3, F25 and F26; Figure 9. a). In contrast, the second group of three faults exhibits multiple displacement maxima downdip of the fault, possibly indicating growth by vertical linkage (F23, F12, and F16; Figure 9. b). Our results show that, regardless of total displacement and/or evidence of growth via vertical linkage, the interval between H3 and H7 has the highest SGR values (SGR >> 20%) for all seven studied faults, whereas the lowest SGR values (SGR << 20%) are found in the Middle to Lower Jurassic interval (between H7 and H8; Figure 13). The Upper to Middle Triassic section shows SGR values of c. 20% (interval between H8 and H10; Figure 13). Below H10, the average SGR value is < 20% across all seven faults (Figure 13). Closer to the lower tip of the fault near H14, we notice a slight increase (to c. 20%) in SGR values (Figure 13).

By comparing the SGR strike-projections of the two groups, we can see that faults in the first (Figure 13. a) have higher overall values than those in the second (Figure 13. b). The differences between the two fault groups are evident by the colours of the strike projections, with faults in the first (Figure 13. a) showing darker colours (SGR >> 20%) than those in the second (SGR << 20%) for a corresponding stratigraphic interval. This visual comparison provides only qualitative evidence for the variability of SGR values between the two fault groups, thus, to further investigate and quantify the differences in fault seal potential between the two fault groups, we analysed SGR values plotted along the length of each fault along the Middle Jurassic Stø

Formation (H7) and Middle Triassic Kobbe Formation (H10). The first four examples (F2, F3, F25 and F26) do not reach or offset Middle Triassic strata, so we only show the SGR analysis along the Middle Jurassic Stø Formation. In contrast, the other three examples (F23, F12 and F16) offset both Middle Triassic and Middle Jurassic rocks. The reason we focus on the Stø and Kobbe formations is because these sandstone-dominated intervals are considered potential CO_2 reservoirs (NPD, 2023).

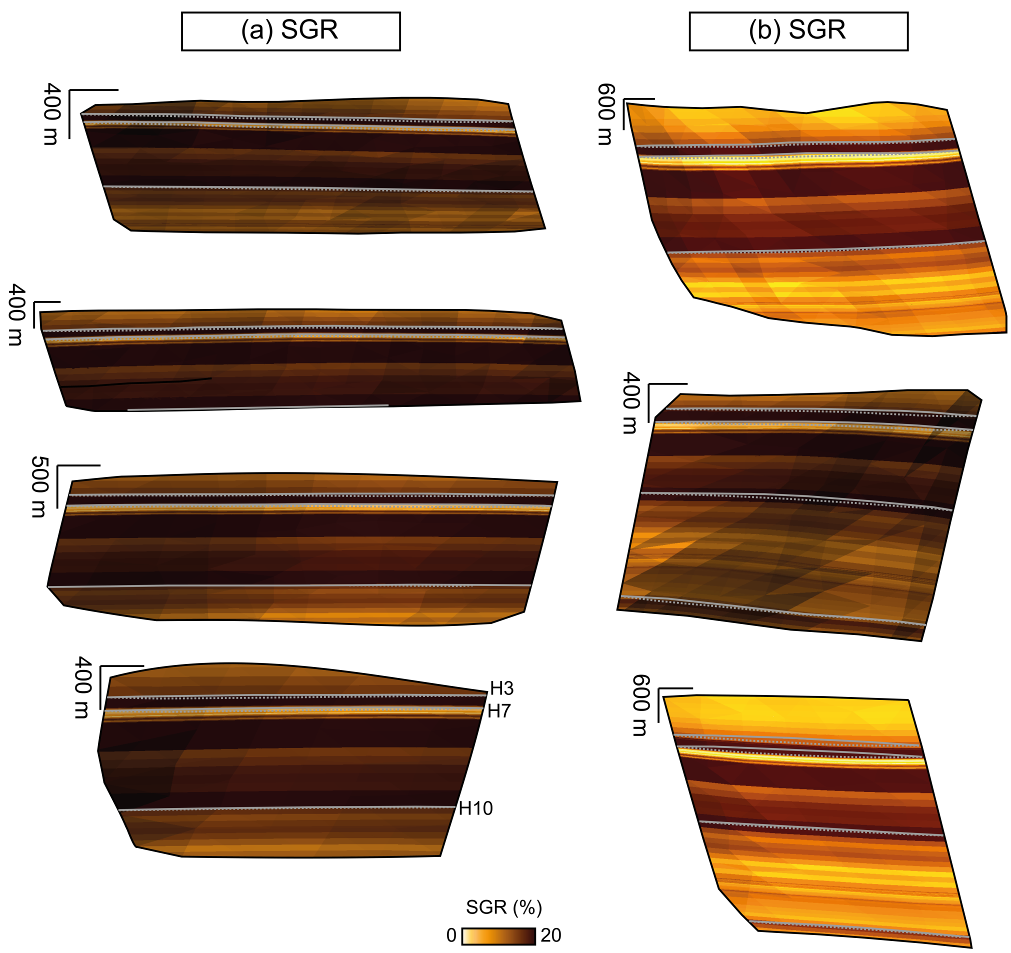

Figure 13. Strike-projected SGR value distribution along the fault surface. The four fault examples shown in **(a) (a.i)** Fault 2, **(a.ii)** Fault 3, **(a.iii)** Fault 25, and **(a.iv)** Fault 26 represent faults with no evidence of vertical linkage. The three fault examples shown in **(b) (b.i)** Fault 23, **(b.ii)** Fault 12, and **(b.iii)** Fault 16 represent faults with evidence of vertical linkage. Three key horizons (H3, H7, and H10) are indicated by light grey lines on the strike-projections (a) & (b).

All four faults (F2, F3, F25 and F26) are likely presently leaking (i.e., SGR << 20%) along their entire lengths (Figure 14. a. i - d. i). The only exception to this is near the faults' lateral tips where displacement approaches zero and SGR values increase (Figure 14. a. i - d. i). However, by examining SGR during the Middle Jurassic (i.e., by using the backstripped displacement), we notice increased lateral variability in fault seal potential between faults and within individual faults (Figure 14. a. ii - d. ii). For example, only half of F2 was likely leaking at this time, with the remaining portion of the fault being likely sealing or exhibiting SGR values transitional between 20 and 40% (Figure 14. a. i, a. ii). In contrast, F26 was likely sealing during the Middle Jurassic along its entire length, compared to being entirely leaking at present-day (Figure 14. d. i, d. ii).

Similar to the first four fault examples, the second group of faults (F23, F12, and F16) are all likely presently leaking (i.e., SGR << 20%) across the Middle Jurassic Stø Formation, along their entire lengths (Figure 15. a. i – c. i). However, unlike the first group, the second group (F23, F12, and F16) appear to be presently sealing across the Middle Triassic Kobbe Formation (Figure 15. a. iii – c. iii). The sealing potential of these fault (F23, F12, and F16) also varied through time, with faults having leaking and sealing patches along length of the fault in the Middle Jurassic (Figure 15. a. ii – c. ii) and being likely entirely sealing during the Middle Triassic (Figure 15. a. iv – c. iv).

As mentioned earlier in the methods section (3), we calculated V_{shale} using linear and non-linear equations (Appendix. 1). The differences in present-day SGR value arising from these two methods were comparable (i.e., SGR values fell within the same range of sealing or leaking potential; Figures 14. a. i - d. I and 15. a. i - c. i; 15. a. iii-c. iii). However, these two V_{shale} estimation methods resulted in large variabilities in the backstripped SGR values as captured by the uncertainty range in our results (Figures 14 and 15). We note that the absolute SGR values are perhaps less relevant to our study than the overall variations in SGR behaviour between the presented fault examples given the limited wellbore control in the area.

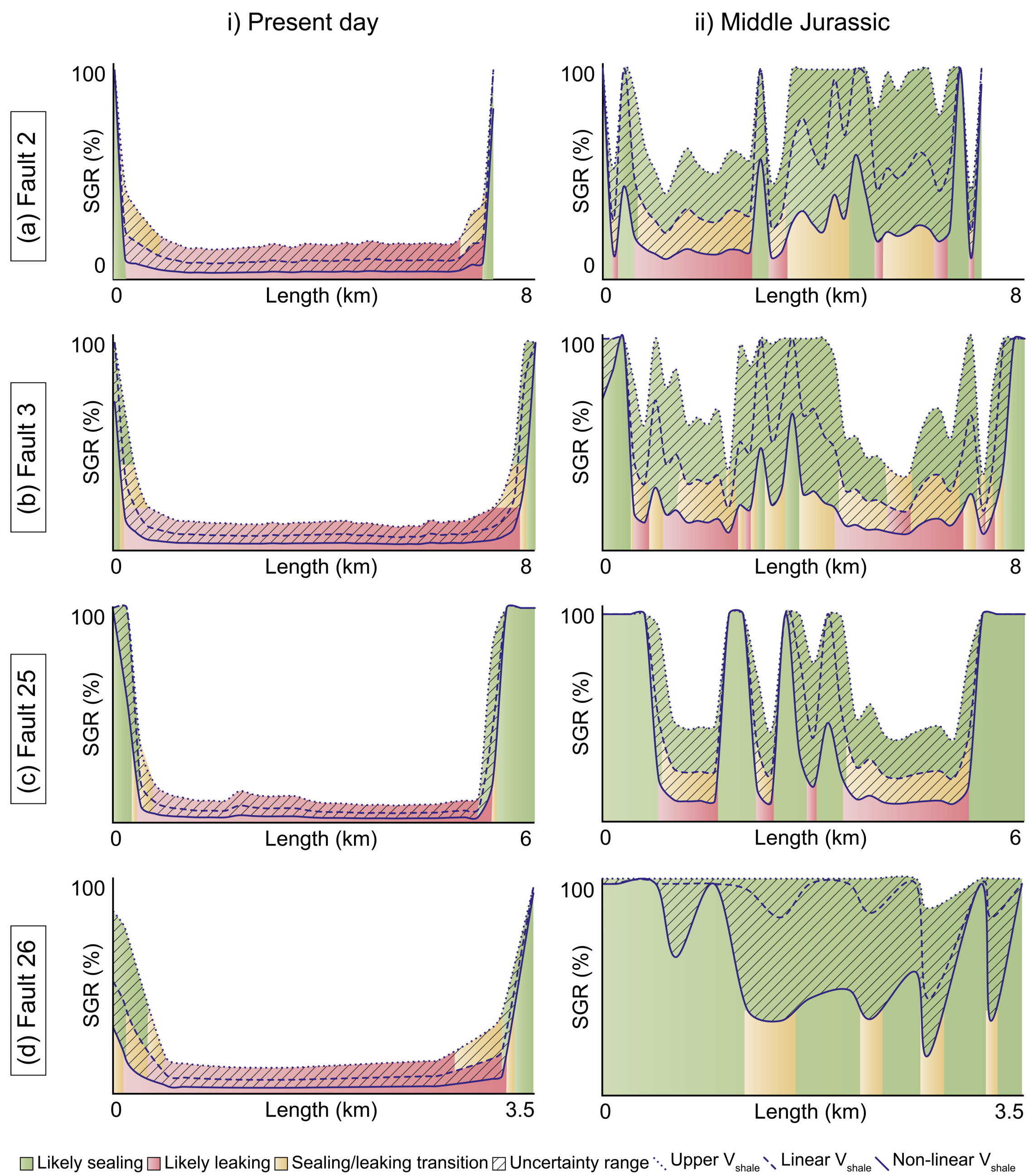

Figure 14. Sealing potential along strike of Fault 2 **(a)**, Fault 3 **(b)**, Fault 25 **(c)**, and Fault 26 **(d)** as expressed by shale gouge ratios (SGR) at present-day **(i)** and at time of deposition **(ii)** using backstripped displacement. The SGR values are estimated using the linear and non-linear V_{shale} equations to represent the uncertainty in calculating SGR values. We use common cut-offs for SGR to represent sealing (SGR > 40), leaking (SGR < 20) potential.

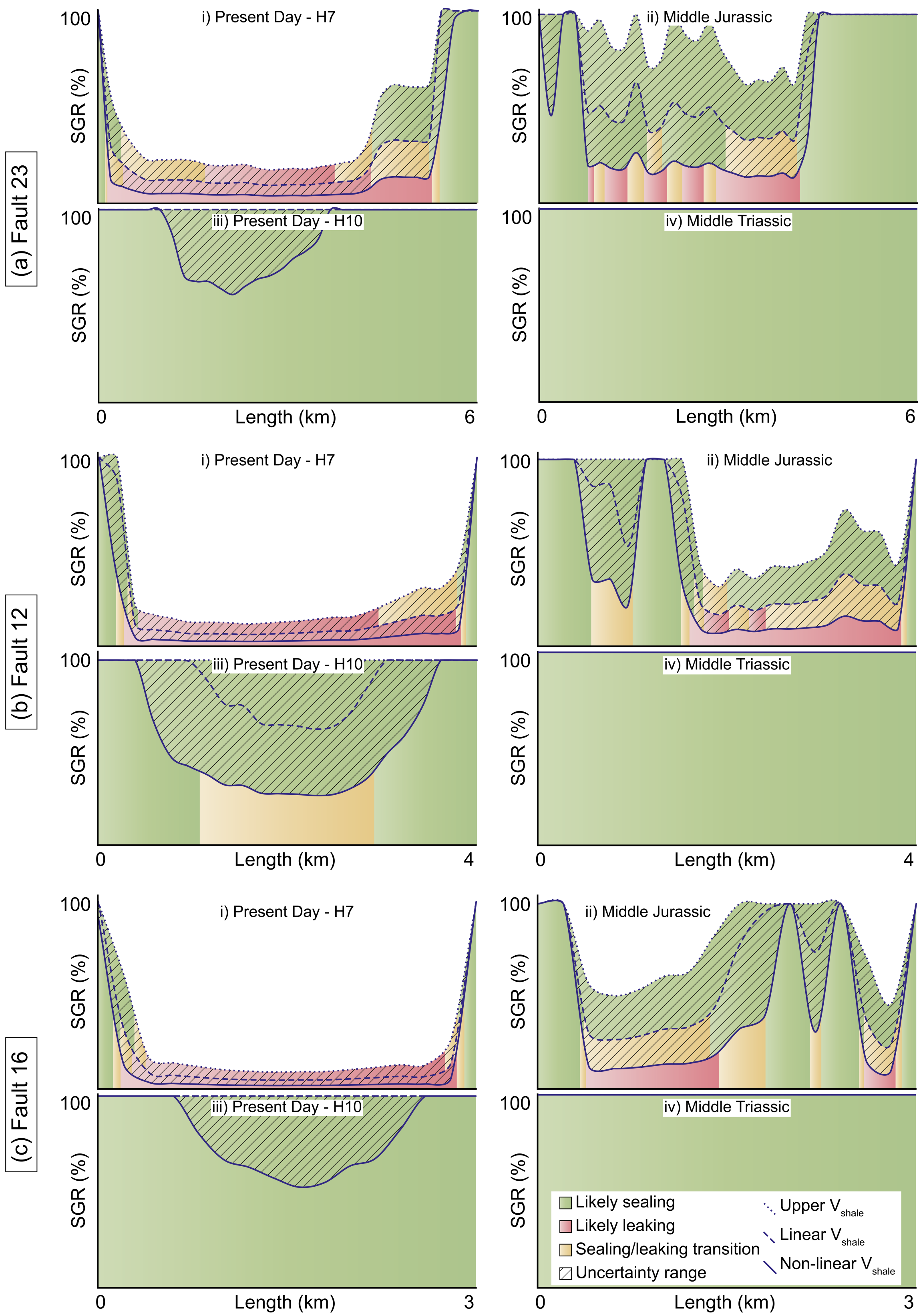

Figure 15. Sealing potential along strike of Fault 23 **(a)**, Fault 12 **(b)**, and Fault 16 **(c)** as expressed by shale gouge ratios (SGR) at present-day along the H7 (Top Stø FM) structural level

(i), at time of deposition of Stø FM during Middle Jurassic **(ii)** using backstripped displacement, at present-day along the H10 (Top Kobbe FM) structural level **(iii),** at time of deposition of Kobbe FM during Middle Triassic **(iv)** using backstripped displacement. . The SGR values are estimated using the linear and non-linear V_{shale} equations to represent the uncertainty in calculating SGR values. We use common cut-offs for SGR to represent sealing (SGR > 40), leaking (SGR < 20) potential.

The way normal faults grow shapes their geometry and internal structure, which control fault rock distribution and juxtaposition relationships, and thus influence the fluid flow properties of fault zones (Yielding et al., 1997; Knipe et al., 1998; Walsh et al., 1998;). Therefore, accurately modelling how faults grow and how they develop through time can significantly contribute towards increasing the predictability of basin models during the exploration stages. It can also improve site characterisation of water aquifers, CO_2 storage and nuclear waste disposal locations, geothermal fields (e.g., Main, 1996; Allmendinger et al., 2000; Sorkhabi & Tsuji, 2005; Rutqvist, 2012; Kaldi et al., 2013; Brune et al., 2017).

5.1 Fault network kinematics and sealing potential

In this study, we focused on the faulting style and development of the fault network in the Samson Dome area, offshore Norway. Overall, we identify four groups of faults. These include, i) faults restricted to the Cretaceous interval (Figures 6. a. i and 7. a, b), ii) faults offsetting Upper Triassic to Lower Cretaceous stratigraphy (Figures 6. a. ii, b and 7. b, c), iii) faults offsetting Middle Triassic to Lower Cretaceous stratigraphy (Figures 6. a. ii, b and 7. b, d, e) and iv) faults offsetting Lower Triassic to Lower Cretaceous (Figures 6. a. ii, b and 7). Isopach analysis indicates that faulting in the Samson Dome developed through multiple phases. The first phase of faulting initiated during the Early to Middle Triassic and formed several NW-SE-striking faults (Figure 10. b). Additionally, we see clear evidence of across-fault thickening by the Late Triassic (Figure 10. d), indicating that the NW-SE-striking faults were active at that time. The second phase of faulting started during the Middle Jurassic and continued into the Early Cretaceous, forming most of the faults in the Samson Dome area (Figure 11. a-b). The multiple phases of fault growth in the Samson Dome are generally consistent with the model proposed by Mattos et al. (2016), where they interpreted an initial phase of faulting in the Middle to Late Triassic and a second phase of faulting to have occurred in the Early to Late Cretaceous.

Another important observation we make is the variable ways in which faults grew. For example, some faults grew via the vertical linkage of segments, something that is defined in our strike-projections by sub-horizontal bands of low displacement (Figure 9). The differences in vertical linkage could be related to the fact some faults experienced reactivation and others did not. Specifically, our results show that faults that experienced vertical linkage represent faults in subset 4 (Figure 6. c), which strike NW-SE and were active since the Early to Middle Triassic, and that were subsequently reactivated during the Late Triassic and Middle Jurassic to Early Cretaceous. The other fault population that shows no evidence of vertical linkage (subset 3; Figure 9. a) corresponds to faults that initiated during the Middle Jurassic to Early Cretaceous (Figure 11. a-b) and that tend to strike almost E-W (Figure 6. c). North Atlantic Ocean opening-related fault reactivation has been proposed by previous studies (e.g., Faleide et al., 1993; 2008; Mattos et al., 2016; Figure 12). However, the opening of the North Atlantic Ocean occurred in the Paleocene – Eocene (e.g., Faleide et al., 2008), some time after the main, Middle Jurassic to Early Cretaceous phase of faulting we document here (Figures 11 and 12). Our results are, however, consistent with those of Mattos et al. (2016), who also concluded faulting commenced in the Late Triassic (Figures 10 and 12), noting that fault initiation might have occurred earlier, during the Early to Middle Triassic (Figure 10. b). The main difference between our results and those of Mattos et al. (2016) is that we show the main period of faulting occurred during the Middle Jurassic to Early Cretaceous, in response to the main rifting phase documented elsewhere in the SW Barents Sea (e.g., Faleide et al., 2008), in contrast to Mattos et al. (2016), who suggests that the majority of fault activity occurred later, in the Late Mesozoic (i.e., Early to Late Cretaceous), in response to the opening of the North Atlantic Ocean (e.g., Faleide et al., 1993; 2008; Mattos et al., 2016).

The value of considering the fault growth history in assessing the potential of faults to seal or leak fluids has recently received increased interest (e.g., Reilly et al., 2017; Song et al., 2020; Michie & Braathen, 2023). While assessing present-day juxtaposition relationships and fault sealing potential is a valuable approach when considering reservoir behaviour over relatively short (i.e., a few tens of years) production timescales, it does not capture the changes that may occur to fault hydraulic properties over longer, geological timescales (e.g., Manzocchi et al., 2010; Reilly et al., 2017). For example, Reilly et al. (2017) show that, despite being likely sealing at present, the Cape Egmont Fault, offshore New Zealand experienced sand-against-sand juxtaposition and was likely leaking at an earlier phase of its development. Our fault seal analysis results reveal that relative differences in SGR values correlate with fault growth patterns. Specifically, we show that the faults associated with vertical linkage and possible reactivation show lower SGR values on average, indicating that they are more likely to leak than other faults within the network (Figure 13). The reason for this is that SGR is inversely proportional to fault throw (Fristad et al., 1997; Yielding et al., 1997; Freeman et al., 1998). Hence, if we keep the thickness of the faulted strata and their V_{shale} content constant, faults with more throw (or displacement) will have lower SGR values. In fact, these reactivated faults (subset 4) are predominately found at the crest of the Samson Dome (Figure 6. c.i), above which there is seismic reflection evidence for fluid leakage and the accumulation of shallow gas (e.g., Vadakkepuliyambatta et al., 2013). In contrast, the faults that appear *not* to have been reactivated and that do *not* show evidence of vertical linkage are characterised by higher SGR values relative to the other faults (Figure 13). In fact, fault reactivation is one of the factors that is thought to influence the fault seal potential (e.g., Bailey et al., 2006), which might explain the variability we observe here.

V_{shale} calculation methods have major implications for fault seal analysis algorithms since differences in those methods will cause inconsistency in the fault seal analysis results (e.g., Yielding, 2002). Our results show that the variations between V_{shale} calculation methods are more significant for low displacement (i.e., < 20 m) faults. The Middle Jurassic and Middle Triassic SGR values for our fault examples demonstrate that depending on method used, a given fault may be potentially sealing or leaking (Figures 14 and 15). In contrast, for faults with larger displacement (i.e., > 20 m), the variations between V_{shale} calculation methods are less significant on the resulting SGR value and inferred sealing potential. These results likely reflect the uncertainty and poorly constrained nature of the V_{shale} calculations. Higher displacement faults are expected to have wider fault damage zones (e.g., Torabi et al., 2020). However, the lithology of the faulted rocks has been shown to have an impact on the width, mechanical and petrophysical properties of their related fault zone (e.g., Torabi et al., 2020). Therefore, in our study, higher displacement could be associated with higher or lower V_{shale} value (i.e., higher, or lower SGR values). In the absence of better constraints on V_{shale} calculations, our SGR results are thus largely driven by changes in displacement and are less sensitive to changes in lithology or V_{shale} values. Hence, the SGR results presented here are highly uncertain and need to be better constrained by additional wellbore and lithology control.

5.2 Timing and origin of the Samson Dome

Previous studies of the Samson Dome use gravity data, 2D and 3D time-migrated seismic reflection data to infer that it is underlain by a several km-thick, at least 12 km-wide, lenticular body of Permian salt (e.g., Breivik et al., 1995; Mattos et al., 2016). This body has a moderately convex-up upper surface, which is parallel to overlying strata within the dome, whereas its basal surface is convex-down, and seemingly discordant and possibly even displaying an erosional relationship with underlying and adjacent strata. In terms of the timing and evolution of the structure, Mattos et al. (2016) suggest that the (moderately well-layered, low-amplitude) Permian salt body was isolated, being somehow encased in (well-layered, high-amplitude) carbonate platform deposits, and that the main period of salt mobilisation in the Early-to-Late Cretaceous resulted from the reactivation of basement faults (not shown in their Figure 13) and to a lesser degree, differential loading imposed by NW-prograding shelf deposits. Similar pockets of low-amplitude seismic facies, flanked by high-amplitude reflections, are observed in seismic reflection data northeast of the Samson Dome near the Swaen Graben (Figure 2, X to X'), where they which might document salt pillows or remnant salt deposits related to salt withdrawal (e.g., Jackson & Talbot, 1986; Nilsen et al., 1995; Koyi, 1998; Jackson & Hudec, 2005; Hudec & Jackson, 2007; Pichel et al., 2018; Rojo et al., 2019). Mattos et al. (2016) then suggest that subsequent deflation and collapse of the dome, during the latest Cretaceous and following a period of quiescence, was driven by a combination of salt dissolution and sediment loading. The preferred model in the literature for the formation of the domes in the SW Barents involves contractional buckling triggered by tectonic inversion during the Late Triassic (Hassaan et al., 2020).

Our study suggest that such a salt body is absent below the Samson Dome, at least based on the apparent lack of a chaotic, poorly reflective seismic facies that might characterise salt that if not diapiric, had at least flowed to inflate beneath and elevate the overburden (e.g., Clark et al., 1998; Jackson & Lewis, 2012; Jones & Davison, 2014; Hassaan et al., 2021). The top of the inferred salt body is convex-up and parallel to overlying strata, consistent with the interpretation of Mattos et al. (2016). However, we cannot infer the geometry of the basal surface of the salt body because of the poor data quality and imaging extent at the depth of the Late Permian - Early Triassic strata (c. 5.5 – 6 km depth). Instead, we observe a low-amplitude, moderately well-layered seismic facies (consistent with Figures 5 and 6 in Mattos et al. 2016), which may be the geophysical expression of layered evaporite and carbonate, rather than pure halite (e.g., Fiduk & Rowan, 2012; Rowan et al., 2019). Indeed, Hassaan et al. (2020) document potentially similar, halite-poor, layered evaporite bodies at the core of several geometrically similar domes in the SW Barents Sea (e.g., Happet dome, Alpha Dome, and Veslekari Dome). However, the basal surfaces of those bodies are flat and not convex-down (Hassaan et al., 2020). The same flat basal surface is often associated with other known salt bodies like the Permian salt deposits in the North Sea (e.g., Clark et al., 1998; Davison et al., 2000; Jackson & Lewis, 2012; Tvedt et al., 2016; Hansen et al., 2021). Even if sufficient halite (the most mobile lithology within layered evaporite sequences; e.g., Jackson et al., 2014, 2019; Rowan et al. 2020) was present in the Permian deposits beneath the Samson Dome, there are some geometric and more critically, mechanical challenges to this model. First, it is unclear why salt might spontaneously flow and inflate, having not moved between the Late Carboniferous/Early Permian and Early Cretaceous (i.e., the time between salt deposition and the main stage of halokinesis proposed by Mattos et al., 2016). This would imply that for 150 Myr, in a tectonically active basin characterised by complex patterns of sediment dispersal (e.g., Faleide et al., 1984; 2008; 2015; Gabrielsen, 1984; Gabrielsen et al., 2016), the salt was not subjected to any gravitational instabilities driven by tilting (i.e., gravity) or differential loading. Related to this, it is highly unlikely that pure salt inflation, in the absence of coeval salt-detached shortening (see below), might lift a very thick (4-5 km), rigid overburden, such as that characterised by the Triassic to Cretaceous succession. Active diapirism, of the type described by Mattos et al. (2016) can only occur below a relatively thin (<500 m) overburden, where salt can rise buoyantly due to it being less dense than its overburden. Salt flow below a thick overburden is however possible during horizontal compression and shortening, with salt anticlines and pillows forming in the core of buckle folds (e.g., Hudec & Jackson, 2007; Dooley et al., 2009). However, in the case of the Samson Dome it is not clear which regional tectonic events might have driven shortening during the Late Triassic or Late Cretaceous, nor why shortening might lead to formation of a sub-circular structure (i.e., a salt pillow), when more commonly elongate structures form (i.e., salt anticlines) (e.g., Hudec & Jackson, 2007; Dooley et al., 2009). Likewise, progradational loading, of the type suggested by Mattos et al. (2016), would likely lead to the formation of elongate rather than sub-circular structures (e.g., Precaspian; e.g., Fernandez et al., 2017; Jackson et al., 2020; Paradox Basin; e.g., Trudgill, 2011; Santos Basin; e.g., Fiduk & Rowan, 2012). It is also important to note that salt-detached shortening and progradational loading are most commonly associated with the formation of salt structures (anticlines or pillows) that have flat rather than convex-down, seemingly erosional base of the type described by Mattos et al. (2016). It is unclear how slip or pre-existing relief along linear basement-involved, sub-salt faults (Mattos et al. 2016) would trigger the differential flow of overlying salt and the formation of a sub-circular structure such as a salt pillow. Finally, we see no evidence in the seismic reflection data for dissolution of salt underlying the Samson Dome. It is also unclear how sufficient volumes of NaCl-undersaturated (i.e., meteoric-water might percolate downwards through a very thick (c. 5 km) overburden to dissolve the salt (see discussion by Jackson and Lewis, 2013). As such, rather than dissolution, we infer that the supra-salt faults record regional extension and perhaps to a lesser degree, outer-arc bending above the growing dome.

In terms of the timing of formation of the Samson Dome, current models describe the main phase of salt mobilisation to have occurred in the Early to Late Cretaceous, as evidenced by broad anticlines deforming Late Cretaceous strata (e.g., Mattos et al., 2016). However, our thickness maps clearly show thinning from as early as the Late Triassic (Figure 10. c), which suggests that the doming or formation of the anticline began much earlier, during the Late Triassic.

We propose an alternative model for the timing of development of the Samson Dome. More specifically, our results support an earlier timing (i.e., Late Triassic) of dome initiation than previously proposed (i.e., Late Mesozoic or Early to Late Cretaceous; Mattos et al., 2016). Our Late Triassic timing of dome initiation is consistent with regional observations of the formation of similar structures in the SW Barents Sea (e.g., Hassaan et al., 2020). However, the mechanism or mechanisms driving dome formation remain ambiguous. Our observations suggest that the Samson Dome formed through two phases involving a possible ductile layer that caused the inflation of the observed anticline (Figures 10; 11; 12). The nature of the ductile material remains unknown but might consist of a layered evaporite sequence or stratified salt based on the reported negative gravity anomaly (e.g., Breivik et al., 1995; Barrère et al., 2009). While our results support the Late Triassic timing of the dome formation proposed by Hassaan et al. (2020), this model still does not explain the formation of an elliptical dome with radial faults at the crest of the dome. An alternative mechanism that could lead to the development of a dome with a similar geometry to the Samson Dome is what is known as a salt-wing intrusion (sensu Hudec & Jackson, 2006). Salt-wing intrusion involves the placement of a salt wedge along a stratigraphic layer or a thin bed in the adjacent rocks (e.g., Hudec & Jackson, 2006). As the sheet inflates, the roof is lifted, often resulting in the onlap or erosion of the roof strata (e.g., Hudec & Jackson, 2006). This process accounts for the observed onlapping in the Late Triassic and Early Cretaceous along with the Upper Cretaceous – Base Eocene unconformity (Figure 12). However, it is unlikely that a salt-wing intrusion led to the formation of the Samson Dome because of the absence or lack of evidence for a deep thick autochthonous salt layer. Therefore, whilst our results provide an updated timing of the Samson Dome formation, further research into the genesis of the dome is needed.

6 Conclusions

We examine the faulting style, development, and sealing potential of the fault network in the Samson Dome area, SW Barents Sea. The fault network has four groups, each offsetting different stratigraphy from the Cretaceous, Late Triassic-Early Cretaceous, Middle Triassic-Early Cretaceous, and Early Triassic-Early Cretaceous. We propose the fault network evolved through multiple phases. NW-SE-striking faults likely initiated during the Early to Middle Triassic, but establishing their timing and initiation is challenging because of data limitations. Most faults developed during the Middle Jurassic to Early Cretaceous, with Triassic faults remaining active. Faulting ceased in the Late Cretaceous, while doming likely began in the Late Triassic, with evidence of thinning and onlapping patterns. Our observations suggest the structures in the Samson Dome area resulted from two faulting (Late Triassic and Middle Jurassic to Early Cretaceous) and two doming (Late Triassic and Late Cretaceous) phases. However, existing halokinetic models do not account for the absence of salt tectonic structures, indicating the need for further research on dome genesis. Fault seal analysis reveals that SGR values correlate with fault growth patterns. Faults associated with vertical linkage and potential reactivation show lower SGR values, suggesting a higher likelihood of leakage compared to other faults. Faults without evidence of reactivation or vertical linkage display higher SGR values, indicating better sealing potential. Variations in V_{shale} calculation methods have significant implications for fault seal analysis, particularly for low displacement faults. In summary, our study provides insights into faulting, development, and sealing potential in the Samson Dome area. It proposes an updated timing for dome formation and highlights the need for further research into the driving mechanism behind the development of the Samson Dome. Consideration of V_{shale} calculation methods is crucial for reliable fault seal analysis.

Acknowledgments

The results presented here are part of AA's PhD research at Imperial College London, funded by Saudi Aramco. We thank the Norwegian Petroleum Directorate for the publicly available data (https://portal.diskos.cgg.com/whereoil-data/) and Schlumberger for Petrel software. We would like to thank the Landscapes and Basins Research group at Imperial College London, specifically Gabriela Salomao Martins, for their valuable contributions and insightful discussions during the various stages of preparing this work.

Open Research

The seismic and wellbore data are openly available in the Norwegian national data repository for petroleum data at https://portal.diskos.cgg.com/whereoil-data/.

References

Alghuraybi, A., Bell, R. E., & Jackson, C. A. L. (2022). The geometric and temporal evolution of fault-related folds constrain normal fault growth patterns, Barents Sea, offshore Norway. *Basin Research*, *34*(2), 618-639. https://doi.org/10.1111/bre.12633

Alghuraybi, A., Bell, R. E., & Jackson, C. A. L. (2023a). A snapshot of the earliest stages of normal fault growth. *Tektonika*, *1*(2), 11-31.

Alghuraybi, A., Bell, R., Jackson, A-L., C. (2023b). Full-waveform inversion as a tool to predict fault zone properties [Preprint]. *EarthArXiv*, [last accessed 01 September 2023].

Ahlborn, M., Stemmerik, L., & Kalstø, T. K. (2014). 3D seismic analysis of karstified interbedded carbonates and evaporites, Lower Permian Gipsdalen Group, Loppa High, southwestern Barents Sea. *Marine and Petroleum Geology*, *56*, 16-33. https://doi.org/10.1016/j.marpetgeo.2014.02.015

Allan, U. S. (1989). Model for hydrocarbon migration and entrapment within faulted structures. *AAPG bulletin*, *73*(7), 803-811. https://doi.org/10.1306/44B4A271-170A-11D7-8645000102C1865D

Allmendinger, R. W., & Shaw, J. H. (2000). Estimation of fault propagation distance from fold shape: Implications for earthquake hazard assessment. Geology, 28(12), 1099-1102. https://doi.org/10.1130/0091-7613(2000)28%3C1099:EOFPDF%3E2.0.CO;2

Argentino, C., Waghorn, K. A., Vadakkepuliyambatta, S., Polteau, S., Bünz, S., & Panieri, G. (2021). Dynamic and history of methane seepage in the SW Barents Sea: new insights from Leirdjupet Fault Complex. *Scientific Reports*, *11*(1), 1-13. https://doi.org/10.1038/s41598-021-83542-0

Bailey, W. R., Underschultz, J., Dewhurst, D. N., Kovack, G., Mildren, S., & Raven, M. (2006). Multi-disciplinary approach to fault and top seal appraisal; Pyrenees–Macedon oil and gas fields, Exmouth Sub-basin, Australian Northwest Shelf. *Marine and Petroleum Geology*, *23*(2), 241-259. https://doi.org/10.1016/j.marpetgeo.2005.08.004

Barrère, C., Ebbing, J., & Gernigon, L. (2009). Offshore prolongation of Caledonian structures and basement characterisation in the western Barents Sea from geophysical modelling. *Tectonophysics*, *470*(1-2), 71-88. https://doi.org/10.1016/j.tecto.2008.07.012

Bouvier, J. D., Kaars-Sijpesteijn, C. H., Kluesner, D. F., Onyejekwe, C. C., & Van der Pal, R. C. (1989). Three-dimensional seismic interpretation and fault sealing investigations, Nun River Field, Nigeria. *AAPG bulletin*, *73*(11), 1397-1414. https://doi.org/10.1306/44B4AA5A-170A-11D7-8645000102C1865D

Breivik, A. J., Gudlaugsson, S. T., & Faleide, J. I. (1994). Ottar Basin, SW Barents Sea: a major Upper Palaeozoic rift basin containing large volumes of deeply buried salt. *Basin research*, *7*(4), 299-312. https://doi.org/10.1111/j.1365-2117.1995.tb00119.x

Bretan, P., Yielding, G., & Jones, H. (2003). Using calibrated shale gouge ratio to estimate hydrocarbon column heights. *AAPG Bulletin, 87*(3), 397-413. https://doi.org/10.1306/08010201128

Brune, S., Williams, S. E., & Mueller, R. D. (2017). Potential links between continental rifting, CO2 degassing and climate change through time. Nature Geoscience, 10(12), 941-946. https://doi.org/10.1038/s41561-017-0003-6

Carruthers, D., Cartwright, J., Jackson, M. P., & Schutjens, P. (2013). Origin and timing of layer-bound radial faulting around North Sea salt stocks: New insights into the evolving stress state around rising diapirs. *Marine and Petroleum Geology*, *48*, 130-148. https://doi.org/10.1016/j.marpetgeo.2013.08.001

Cartwright, J. A., Trudgill, B. D., & Mansfield, C. S. (1995). Fault growth by segment linkage: an explanation for scatter in maximum displacement and trace length data from the Canyonlands Grabens of SE Utah. *Journal of structural Geology*, *17*(9), 1319-1326. https://doi.org/10.1016/0191-8141(95)00033-A

Childs, C., Nicol, A., Walsh, J. J., & Watterson, J. (2003). The growth and propagation of synsedimentary faults. *Journal of Structural geology*, *25*(4), 633-648. https://doi.org/10.1016/S0191-8141(02)00054-8

Childs, C. J. J. P., Walsh, J. J., & Watterson, J. (1997). Complexity in fault zone structure and implications for fault seal prediction. In *Norwegian petroleum society special publications* (Vol. 7, pp. 61-72). Elsevier. https://doi.org/10.1016/S0928-8937(97)80007-0

Clark, J. A., Stewart, S. A., & Cartwright, J. A. (1998). Evolution of the NW margin of the North Permian Basin, UK North Sea. *Journal of the Geological Society*, *155*(4), 663-676. https://doi.org/10.1144/gsjgs.155.4.0663

Clavier, C., Hoyle, W., & Meunier, D. (1971). Quantitative interpretation of thermal neutron decay time logs: part I. Fundamentals and techniques. *Journal of Petroleum Technology*, *23*(06), 743-755. https://doi.org/10.2118/2658-A-PA

Davison, I., Alsop, G. I., Evans, N. G., & Safaricz, M. (2000). Overburden deformation patterns and mechanisms of salt diapir penetration in the Central Graben, North Sea. *Marine and Petroleum Geology*, *17*(5), 601-618. https://doi.org/10.1016/S0264-8172(00)00011-8

Di Lucia, M., Sayago, J., Frijia, G., Cotti, A., Sitta, A., & Mutti, M. (2017). Facies and seismic analysis of the Late Carboniferous–Early Permian Finnmark carbonate platform (southern

Norwegian Barents Sea): An assessment of the carbonate factories and depositional geometries. Marine and Petroleum Geology, 79, 372-393. https://doi.org/10.1016/j.marpetgeo.2016.10.029

Dockrill, B., & Shipton, Z. K. (2010). Structural controls on leakage from a natural CO2 geologic storage site: Central Utah, USA. *Journal of Structural Geology*, *32*(11), 1768-1782. https://doi.org/10.1016/j.jsg.2010.01.007

Doré, A. G. (1995). Barents Sea Geology, Petroleum Resources and Commercial Potential. *Arctic*, *48*(3), 207–221. http://www.jstor.org/stable/40511656

Doré, A. G., & Jensen, L. N. (1996). The impact of late Cenozoic uplift and erosion on hydrocarbon exploration: offshore Norway and some other uplifted basins. *Global and Planetary Change*, *12*(1-4), 415-436. https://doi.org/10.1016/0921-8181(95)00031-3

Edmundson, I., Rotevatn, A., Davies, R., Yielding, G., & Broberg, K. (2020). Key controls on hydrocarbon retention and leakage from structural traps in the Hammerfest Basin, SW Barents Sea: implications for prospect analysis and risk assessment. *Petroleum Geoscience*, *26*(4), 589-606. https://doi.org/10.1144/petgeo2019-094

Eldholm, O., & Thiede, J. (1980). Cenozoic continental separation between Europe and Greenland. Palaeogeography, Palaeoclimatology, *Palaeoecology, 30*(C), 243–259. https://doi.org/10.1016/0031-0182(80)90060-7

Elvebakk, G., Hunt, D. W., & Stemmerik, L. (2002). From isolated buildups to buildup mosaics: 3D seismic sheds new light on upper Carboniferous–Permian fault controlled carbonate buildups, Norwegian Barents Sea. *Sedimentary Geology*, *152*(1-2), 7-17. https://doi.org/10.1016/S0037-0738(02)00232-4

Faleide, J. I., Tsikalas, F., Breivik, A. J., Mjelde, R., Ritzmann, O., Engen, Ø., Wilson, J., & Eldholm, O. (2008). Structure and evolution of the continental margin off Norway and the Barents Sea. *Episodes, 31*(1), 82–91. https://doi.org/10.18814/epiiugs/2008/v31i1/012

Faleide, Jan I., Vågnes, E., & Gudlaugsson, S. T. (1993). Late Mesozoic-Cenozoic evolution of the south-western Barents Sea in a regional rift-shear tectonic setting. *Marine and Petroleum Geology*, *10*(3), 186–214. https://doi.org/10.1016/0264-8172(93)90104-Z

Faleide, Jan Inge, Gudlaugsson, S. T., & Jacquart, G. (1984). Evolution of the western Barents Sea. *Marine and Petroleum Geology*, *1*(2), 70–78. https://doi.org/10.1016/0264-8172(84)90082-5

Fernandez, N., Duffy, O. B., Hudec, M. R., Jackson, M. P., Burg, G., Jackson, C. A. L., & Dooley, T. P. (2017). The origin of salt-encased sediment packages: Observations from the SE Precaspian Basin (Kazakhstan). *Journal of Structural Geology*, *97*, 237-256. https://doi.org/10.1016/j.jsg.2017.01.008

Fiduk, J. C., & Rowan, M. G. (2012). Analysis of folding and deformation within layered evaporites in Blocks BM-S-8 &-9, Santos Basin, Brazil. *Geological Society, London, Special Publications*, *363*(1), 471-487. https://doi.org/10.1144/SP363.22

Fisher, Q. J., & Jolley, S. J. (2007). Treatment of faults in production simulation models. *Geological Society, London, Special Publications*, *292*(1), 219-233. https://doi.org/10.1144/SP292.13

Fisher, Q. J., Haneef, J., Grattoni, C. A., Allshorn, S., & Lorinczi, P. (2018). Permeability of fault rocks in siliciclastic reservoirs: Recent advances. Marine and Petroleum Geology, 91, 29-42. https://doi.org/10.1016/j.marpetgeo.2017.12.019

Fossen, H., & Bale, A. (2007). Deformation bands and their influence on fluid flow. *AAPG bulletin*, *91*(12), 1685-1700. https://doi.org/10.1306/07300706146

Freeman, B., Yielding, G., Needham, D. T., & Badley, M. E. (1998). Fault seal prediction: the gouge ratio method. *Geological Society, London, Special Publications*, *127*(1), 19-25. https://doi.org/10.1144/GSL.SP.1998.127.01.03

Fristad, T. A. G. B. P., Groth, A., Yielding, G., & Freeman, B. (1997). Quantitative fault seal prediction: a case study from Oseberg Syd. In *Norwegian petroleum society special publications* (Vol. 7, pp. 107-124). Elsevier. https://doi.org/10.1016/S0928-8937(97)80010-0

Fulljames, J. R., Zijerveld, L. J. J., & Franssen, R. C. M. W. (1997). Fault seal processes: systematic analysis of fault seals over geological and production time scales. In *Norwegian Petroleum Society Special Publications* (Vol. 7, pp. 51-59). Elsevier. https://doi.org/10.1016/S0928-8937(97)80006-9

Gabrielsen, R. H. (1984). Long-lived fault zones and their influence on the tectonic development of the southwestern Barents Sea. *Journal of the Geological Society*, *141*(4), 651–662. https://doi.org/10.1144/gsjgs.141.4.0651

Gabrielsen, R. H., & Kløvjan, O. S. (1997). Late Jurassic—early Cretaceous caprocks of the southwestern Barents Sea: fracture systems and rock mechanical properties. In *Norwegian Petroleum Society Special Publications* (Vol. 7, pp. 73-89). Elsevier. https://doi.org/10.1016/S0928-8937(97)80008-2

Gabrielsen, R. H., Faerseth, R. B., & Jensen, L. N. (1990). *Structural elements of the Norwegian continental shelf. Pt. 1. The Barents Sea region*. Norwegian Petroleum Directorate. https://www.npd.no/globalassets/1-npd/publikasjoner/npd-bulletins/npd-bulletin-6-1990.pdf

Gabrielsen, Roy H., Sokoutis, D., Willingshofer, E., & Faleide, J. I. (2016). Fault linkage across weak layers during extension: An experimental approach with reference to the Hoop Fault Complex of the SW Barents Sea. *Petroleum Geoscience*, *22*(2), 123–135. https://doi.org/10.1144/petgeo2015-029

Gawthorpe, R. L., & Leeder, M. R. (2000). Tectono-sedimentary evolution of active extensional basins. *Basin Research*, *12*(3-4), 195-218. https://doi.org/10.1111/j.1365-2117.2000.00121.x

Gawthorpe, R. L., Jackson, C. A. L., Young, M. J., Sharp, I. R., Moustafa, A. R., & Leppard, C. W. (2003). Normal fault growth, displacement localisation and the evolution of normal fault populations: the Hammam Faraun fault block, Suez rift, Egypt. *Journal of Structural Geology*, *25*(6), 883-895. https://doi.org/10.1016/S0191-8141(02)00088-3

Giba, M., Walsh, J. J., & Nicol, A. (2012). Segmentation and growth of an obliquely reactivated normal fault. *Journal of Structural Geology*, *39*, 253-267. https://doi.org/10.1016/j.jsg.2012.01.004

Glørstad-Clark, E., Faleide, J. I., Lundschien, B. A., & Nystuen, J. P. (2010). Triassic seismic sequence stratigraphy and paleogeography of the western Barents Sea area. *Marine and Petroleum Geology*, *27*(7), 1448–1475. https://doi.org/10.1016/j.marpetgeo.2010.02.008

Grimstad, S., (2016). Salt tectonics in the central and northeastern Nordkapp Basin, Barents Sea, Master's thesis, University of Oslo, Oslo, Norway.

Gudlaugsson, S. T., Faleide, J. I., Johansen, S. E., & Breivik, A. J. (1998). Late Palaeozoic structural development of the south-western Barents Sea. *Marine and Petroleum Geology*, *15*(1), 73-102. https://doi.org/10.1016/S0264-8172(97)00048-2

Gupta, S., Underhill, J. R., Sharp, I. R., & Gawthorpe, R. L. (1999). Role of fault interactions in controlling synrift sediment dispersal patterns: Miocene, Abu Alaqa Group, Suez Rift, Sinai, Egypt. *Basin Research*, *11*(2), 167. https://doi.org/10.1046/j.1365-2117.1999.00300.x

Hansen, T. H., Clausen, O. R., & Andresen, K. J. (2021). Thick-and thin-skinned basin inversion in the Danish Central Graben, North Sea–the role of deep evaporites and basement kinematics. *Solid Earth*, *12*(8), 1719-1747. https://doi.org/10.5194/se-12-1719-2021

Harishidayat, D., Omosanya, K. O., & Johansen, S. E. (2015). 3D seismic interpretation of the depositional morphology of the Middle to Late Triassic fluvial system in Eastern Hammerfest Basin, Barents Sea. *Marine and Petroleum Geology*, *68*(November 2017), 470–479. https://doi.org/10.1016/j.marpetgeo.2015.09.007

Hassaan, M., Faleide, J. I., Gabrielsen, R. H., & Tsikalas, F. (2020). Carboniferous graben structures, evaporite accumulations and tectonic inversion in the southeastern Norwegian Barents Sea. Marine and Petroleum Geology, 112, 104038. https://doi.org/10.1016/j.marpetgeo.2019.104038

Hassaan, M., Faleide, J. I., Gabrielsen, R. H., & Tsikalas, F. (2021). Effects of basement structures and Carboniferous basin configuration on evaporite distribution and the development of salt structures in Nordkapp Basin, Barents Sea—Part I. *Basin Research*, *33*(4), 2474-2499. https://doi.org/10.1111/bre.12565

Heidbach, O., Rajabi, M., Reiter, K., Ziegler, M., & Wsm Team. (2016). World stress map database release 2016. *GFZ Data Services*, *10*. doi:10.5880/WSM.2016.001

Hermanrud, C., Halkjelsvik, M. E., Kristiansen, K., Bernal, A., & Strömbäck, A. C. (2014). Petroleum column-height controls in the western Hammerfest Basin, Barents Sea. *Petroleum Geoscience*, *20*(3), 227-240. https://doi.org/10.1144/petgeo2013-041

Hooper, E. C. D. (1991). Fluid migration along growth faults in compacting sediments. *Journal of Petroleum Geology*, *14*, 161-180. https://doi.org/10.1111/j.1747-5457.1991.tb00360.x

Hudec, M. R., & Jackson, M. P. (2007). Terra infirma: Understanding salt tectonics. *Earth-Science Reviews*, *82*(1-2), 1-28. https://doi.org/10.1016/j.earscirev.2007.01.001

Jackson, C. A. L., & Rotevatn, A. (2013). 3D seismic analysis of the structure and evolution of a salt-influenced normal fault zone: a test of competing fault growth models. *Journal of Structural Geology*, *54*, 215-234. https://doi.org/10.1016/j.jsg.2013.06.012

Jackson, C. A. L., Bell, R. E., Rotevatn, A., & Tvedt, A. B. (2017). Techniques to determine the kinematics of synsedimentary normal faults and implications for fault growth models. *Geological Society, London, Special Publications*, *439*(1), 187-217. https://doi.org/10.1144/SP439.22

Jackson, C. A. L., Duffy, O. B., Fernandez, N., Dooley, T. P., Hudec, M. R., Jackson, M. P., & Burg, G. (2020). The stratigraphic record of minibasin subsidence, Precaspian Basin, Kazakhstan. *Basin Research*, *32*(4), 739-763. https://doi.org/10.1111/bre.12393

Jackson, M. P., & Hudec, M. R. (2005). Stratigraphic record of translation down ramps in a passive-margin salt detachment. *Journal of Structural Geology*, *27*(5), 889-911. https://doi.org/10.1016/j.jsg.2005.01.010

Jackson, C. A. L., & Lewis, M. M. (2012). Origin of an anhydrite sheath encircling a salt diapir and implications for the seismic imaging of steep-sided salt structures, Egersund Basin, Northern North Sea. *Journal of the Geological Society*, *169*(5), 593-599. https://doi.org/10.1144/0016-76492011-126

Jackson, M. P., & Talbot, C. J. (1986). External shapes, strain rates, and dynamics of salt structures. *Geological Society of America Bulletin*, *97*(3), 305-323. https://doi.org/10.1130/0016-7606(1986)97%3C305:ESSRAD%3E2.0.CO;2

Jensen, L. N., & Sørensen, K. (1992). Tectonic framework and halokinesis of the Nordkapp Basin, Barents Sea. In *Structural and tectonic modelling and its application to petroleum geology* (pp. 109-120). Elsevier. https://doi.org/10.1016/B978-0-444-88607-1.50012-7

Johansen, S. E., Ostisty, B. K., Birkeland, Fedorovsky, Y. F., Martirosjan, V. N., Christensen, O. B., Cheredeev, S. I., Ignatenko, E. A., & Margulis, L. S. (1993). Hydrocarbon potential in the Barents Sea region: Play distribution and potential. In *Norwegian Petroleum Society Special Publications* (Vol. 2, Issue C, pp. 273–320). Elsevier. https://doi.org/10.1016/B978-0-444-88943-0.50024-1

Jolley, S. J., Fisher, Q. J., & Ainsworth, R. B. (2010). Reservoir compartmentalization: an introduction. Geological Society, London, Special Publications, 347(1), 1-8. https://doi.org/10.1144/SP347.1

Jones, I. F., & Davison, I. (2014). Seismic imaging in and around salt bodies. *Interpretation*, *2*(4), SL1-SL20. https://doi.org/10.1190/INT-2014-0033.1

Jones, C. E., Evans, M., Ratcliffe, A., Conroy, G., Jupp, R., Selvage, J. I., & Ramsey, L. (2013, June). Full waveform inversion in a complex geological setting-a narrow azimuth towed streamer case study from the Barents Sea. In *75th EAGE Conference & Exhibition incorporating SPE EUROPEC 2013* (pp. cp-348). EAGE Publications BV. https://doi.org/10.3997/2214-4609.20130830

Kaldi, J., Daniel, R., Tenthorey, E., Michael, K., Schacht, U., Nicol, A., Underschultz, J., & Backe, G. (2013). Containment of CO2 in CCS: Role of Caprocks and Faults. Energy Procedia, 37, 5403-5410. https://doi.org/10.1016/j.egypro.2013.06.458

Knipe, R. J. (1992). Faulting processes and fault seal. In *Structural and tectonic modelling and its application to petroleum geology* (pp. 325-342). Elsevier. https://doi.org/10.1016/B978-0-444-88607-1.50027-9

Knipe, R. J., Jones, G., & Fisher, Q. J. (1998). Faulting, fault sealing and fluid flow in hydrocarbon reservoirs: an introduction. In G. Jones, Q. J. Fisher, & R. J. Knipe (Eds.), *Faulting, Fault Sealing and Fluid Flow in Hydrocarbon Reservoirs* (Vol. 147, pp. vii-xxi). London: Geological Society, London, Special Publications. https://doi.org/10.1144/GSL.SP.1998.147.01.01

Koyi, H. (1998). The shaping of salt diapirs. *Journal of Structural Geology*, *20*(4), 321-338. https://doi.org/10.1016/S0191-8141(97)00092-8

Larssen, G. B., Elvebakk, G., Henriksen, L. B., Nilsson, I., Samuelsberg, T. J., Stemmerik, L., Worsley, D., Kristensen, S. E., & Svånå, T. a. (2002). Upper Palaeozoic lithostratigraphy of the Southern Norwegian Barents Sea. *Norwegian Petroleum Directorate Bulletin*, *9*, 76.

Lathrop, B., Jackson, C., Bell, R. E., & Rotevatn, A. (2022). Displacement/length scaling relationships for normal faults; a review, critique, and revised compilation. https://doi.org/10.31223/X58S7G

Letouzey, J. L. B. C. J., Colletta, B., Vially, R. A., & Chermette, J. C. (1995). Evolution of salt-related structures in compressional settings. In M.P.A. Jackson, D.G. Roberts, & S. Snelson (Eds.), *Salt Tectonics: a Global Perspective* (pp. 41-60), AAPG Memoir. https://doi.org/10.1306/M65604C3

Lezzar, K. E., Tiercelin, J. J., Le Turdu, C., Cohen, A. S., Reynolds, D. J., Le Gall, B., & Scholz, C. A. (2002). Control of normal fault interaction on the distribution of major Neogene sedimentary depocenters, Lake Tanganyika, East African rift. *AAPG bulletin*, *86*(6), 1027-1059. https://doi.org/10.1306/61EEDC1A-173E-11D7-8645000102C1865D

Lindsay, N. G., Murphy, F. C., Walsh, J. J., & Watterson, J. (1992). Outcrop studies of shale smears on fault surface. *The geological modelling of hydrocarbon reservoirs and outcrop analogues*, 113-123. https://doi.org/10.1002/9781444303957.ch6

Main, I. (1996). Statistical physics, seismogenesis, and seismic hazard. Reviews of Geophysics, 34(4), 433-462. https://doi.org/10.1029/96RG02808

Makurat, A., Torudbakken, B., Monsen, K., & Rawlings, C. (1992, October). Cenezoic uplift and caprock seal in the Barents Sea: fracture modelling and seal risk evaluation. In *SPE Annual Technical Conference and Exhibition*. OnePetro. https://doi.org/10.2118/24740-MS

Manzocchi, T., Childs, C., & Walsh, J. J. (2010). Faults and fault properties in hydrocarbon flow models. *Geofluids*, *10*(1-2), 94-113. https://doi.org/10.1111/j.1468-8123.2010.00283.x

Mattos, N. H., Alves, T. M., & Omosanya, K. O. (2016). Crestal fault geometries reveal late halokinesis and collapse of the Samson Dome, Northern Norway: Implications for petroleum systems in the Barents Sea. *Tectonophysics*, *690*, 76-96. https://doi.org/10.1016/j.tecto.2016.04.043

Michie, E. A. H., & Braathen, A. (2023). How displacement analysis may aid fault risking strategies for CO2 storage. *Basin Research*. https://doi.org/10.1111/bre.12807

Mitiku, A. B., & Bauer, S. (2013). Optimal use of a dome-shaped anticline structure for CO 2 storage: a case study in the North German sedimentary basin. *Environmental Earth Sciences*, *70*, 3661-3673.

Mohammedyasin, S. M., Lippard, S. J., Omosanya, K. O., Johansen, S. E., & Harishidayat, D. (2016). Deep-seated faults and hydrocarbon leakage in the Snøhvit Gas Field, Hammerfest Basin, southwestern Barents Sea. *Marine and Petroleum Geology*, *77*, 160-178. https://doi.org/10.1016/j.marpetgeo.2016.06.011

Morley, C. K., Nelson, R. A., Patton, T. L., & Munn, S. G. (1990). Transfer zones in the East African rift system and their relevance to hydrocarbon exploration in rifts. *AAPG bulletin*, *74*(8), 1234-1253. https://doi.org/10.1306/0C9B2475-1710-11D7-8645000102C1865D

Nicol, A., Watterson, J., Walsh, J. J., & Childs, C. (1996). The shapes, major axis orientations and displacement patterns of fault surfaces. *Journal of Structural Geology*, *18*(2-3), 235-248. https://doi.org/10.1016/S0191-8141(96)80047-2

Nilsen, K. T., Vendeville, B. C., & Johansen, J. T. (1995). Influence of regional tectonics on halokinesis in the Nordkapp Basin, Barents Sea, *in* M. P. A. Jackson, D. G. Roberts, and S. Snelson, eds., Salt tectonics: a global perspective: *AAPG Memoir 65*, 413-436.

NPD (2023). *Factpages Wellbore 7224/7-1*. https://factpages.npd.no/en/wellbore/PageView/Exploration/All/1245

Ostanin, I., Anka, Z., di Primio, R., & Bernal, A. (2013). Hydrocarbon plumbing systems above the Snøhvit gas field: structural control and implications for thermogenic methane leakage in the Hammerfest Basin, SW Barents Sea. *Marine and Petroleum Geology*, *43*, 127-146. https://doi.org/10.1016/j.marpetgeo.2013.02.012

Paoletti, V., Milano, M., Baniamerian, J., & Fedi, M. (2020). Magnetic field imaging of salt structures at Nordkapp Basin, Barents Sea. *Geophysical Research Letters*, *47*(18), e2020GL089026. https://doi.org/10.1029/2020GL089026

Pechlivanidou, S., Cowie, P. A., Hannisdal, B., Whittaker, A. C., Gawthorpe, R. L., Pennos, C., & Riiser, O. S. (2018). Source-to-sink analysis in an active extensional setting: Holocene erosion and deposition in the Sperchios rift, central Greece. Basin Research, 30(3), 522-543. https://doi.org/10.1111/bre.12263

Pichel, L. M., Peel, F., Jackson, C. A., & Huuse, M. (2018). Geometry and kinematics of salt-detached ramp syncline basins. *Journal of Structural Geology*, *115*, 208-230. https://doi.org/10.1016/j.jsg.2018.07.016

Rafaelsen, B., Elvebakk, G., Andreassen, K., Stemmerik, L., Colpaert, A., & Samuelsberg, T. J. (2008). From detached to attached carbonate buildup complexes—3D seismic data from the upper Palaeozoic, Finnmark Platform, southwestern Barents Sea. Sedimentary Geology, 206(1-4), 17-32. https://doi.org/10.1016/j.sedgeo.2008.03.001

Randen, T., Pedersen, S. I., & Sønneland, L. (2001). Automatic extraction of fault surfaces from three-dimensional seismic data. *SEG Technical Program Expanded Abstracts*, *20*(1), 551–554. https://doi.org/10.1190/1.1816675

Reilly, C., Nicol, A., Walsh, J. J., & Kroeger, K. F. (2016). Temporal changes of fault seal and early charge of the Maui Gas-condensate field, Taranaki Basin, New Zealand. *Marine and Petroleum Geology*, *70*, 237-250. https://doi.org/10.1016/j.marpetgeo.2015.11.018

Riis, F., & Halland, E. (2014). CO2 Storage Atlas of the Norwegian Continental Shelf: Methods Used to Evaluate Capacity and Maturity of the CO2 Storage Potential. *Energy Procedia*, *63*, 5258-5265. https://doi.org/10.1016/j.egypro.2014.11.557

Ritzmann, O., & Faleide, J. I. (2007). Caledonian basement of the western Barents Sea. *Tectonics*, *26*(5), 1–20. https://doi.org/10.1029/2006TC002059

Rojo, L. A., Cardozo, N., Escalona, A., & Koyi, H. (2019). Structural style and evolution of the Nordkapp Basin, Norwegian Barents Sea. *AAPG Bulletin*, *103*(9), 2177-2217. https://doi.org/10.1306/01301918028

Rojo, L. A., Escalona, A., & Schulte, L. (2016). The use of seismic attributes to enhance imaging of salt structures in the Barents Sea. *First Break*, *34*(11). https://doi.org/10.3997/1365-2397.2016014

Rowan, M. G., & Lindsø, S. (2017). Salt tectonics of the Norwegian Barents Sea and northeast Greenland shelf. In *Permo-Triassic Salt Provinces of Europe, North Africa and the Atlantic Margins* (pp. 265-286). Elsevier. https://doi.org/10.1016/B978-0-12-809417-4.00013-6

Rowan, M. G., Urai, J. L., Fiduk, J. C., & Kukla, P. A. (2019). Deformation of intrasalt competent layers in different modes of salt tectonics. *Solid Earth*, *10*(3), 987-1013. https://doi.org/10.5194/se-10-987-2019

Rutqvist, J. (2012). The geomechanics of CO 2 storage in deep sedimentary formations. Geotechnical and Geological Engineering, 30, 525-551. https://doi.org/10.1007/s10706-011-9491-0

Sharp, I. R., Gawthorpe, R. L., Armstrong, B., & Underhill, J. R. (2000). Propagation history and passive rotation of mesoscale normal faults: implications for synrift stratigraphic development. *Basin Research*, *12*(3-4), 285-305. https://doi.org/10.1111/j.1365-2117.2000.00132.x

Skurtveit, E., Torabi, A., Sundal, A., & Braathen, A. (2021). The role of mechanical stratigraphy on CO2 migration along faults–examples from Entrada Sandstone, Humbug Flats, Utah, USA. *International Journal of Greenhouse Gas Control*, *109*, 103376. https://doi.org/10.1016/j.ijggc.2021.103376

Song, X., Meng, L., Fu, X., Wang, H., Sun, Y., & Jiang, W. (2020). Sealing capacity evolution of trap-bounding faults in sand-clay sequences: insights from present and paleo-oil entrapment in fault-bounded traps in the Qinan area, Bohai Bay Basin, China. *Marine and Petroleum Geology*, *122*, 104680. https://doi.org/10.1016/j.marpetgeo.2020.104680

Sorkhabi, R., & Tsuji, Y. (2005). Faults, fluid flow, and petroleum traps. American Association of Petroleum Geologists. https://doi.org/10.1306/M851033

Trudgill, B. D. (2011). Evolution of salt structures in the northern Paradox Basin: Controls on evaporite deposition, salt wall growth and supra-salt stratigraphic architecture. *Basin Research*, *23*(2), 208-238. https://doi.org/10.1111/j.1365-2117.2010.00478.x

Tvedt, A. B., Rotevatn, A., & Jackson, C. A. (2016). Supra-salt normal fault growth during the rise and fall of a diapir: Perspectives from 3D seismic reflection data, Norwegian North Sea. *Journal of Structural Geology*, *91*, 1-26. https://doi.org/10.1016/j.jsg.2016.08.001

Vadakkepuliyambatta, S., Bünz, S., Mienert, J., & Chand, S. (2013). Distribution of subsurface fluid-flow systems in the SW Barents Sea. *Marine and Petroleum Geology*, *43*, 208-221. https://doi.org/10.1016/j.marpetgeo.2013.02.007

Walsh, J. J., & Watterson, J. (1988). Analysis of the relationship between displacements and dimensions of faults. *Journal of Structural geology*, *10*(3), 239-247. https://doi.org/10.1016/0191-8141(88)90057-0

Walsh, J. J., Watterson, J., Heath, A. E., & Childs, C. (1998). Representation and scaling of faults in fluid flow models. *Petroleum Geoscience*, *4*(3), 241-251. https://doi.org/10.1144/petgeo.4.3.241

Yielding, G. (2002). Shale gouge ratio—Calibration by geohistory. In *Norwegian petroleum society special publications* (Vol. 11, pp. 1-15). Elsevier. https://doi.org/10.1016/S0928-8937(02)80003-0

Yielding, G. (2015). Trapping of buoyant fluids in fault-bound structures. *Geological Society, London, Special Publications*, *421*(1), 29-39. https://doi.org/10.1144/SP421.3

Yielding, G. P. B. S., Bretan, P., & Freeman, B. (2010). Fault seal calibration: a brief review. *Geological Society, London, Special Publications*, *347*(1), 243-255. https://doi.org/10.1144/SP347.14

Yielding, G., Freeman, B., & Needham, D. T. (1997). Quantitative fault seal prediction. *AAPG bulletin*, *81*(6), 897-917. https://doi.org/10.1306/522B498D-1727-11D7-8645000102C1865D

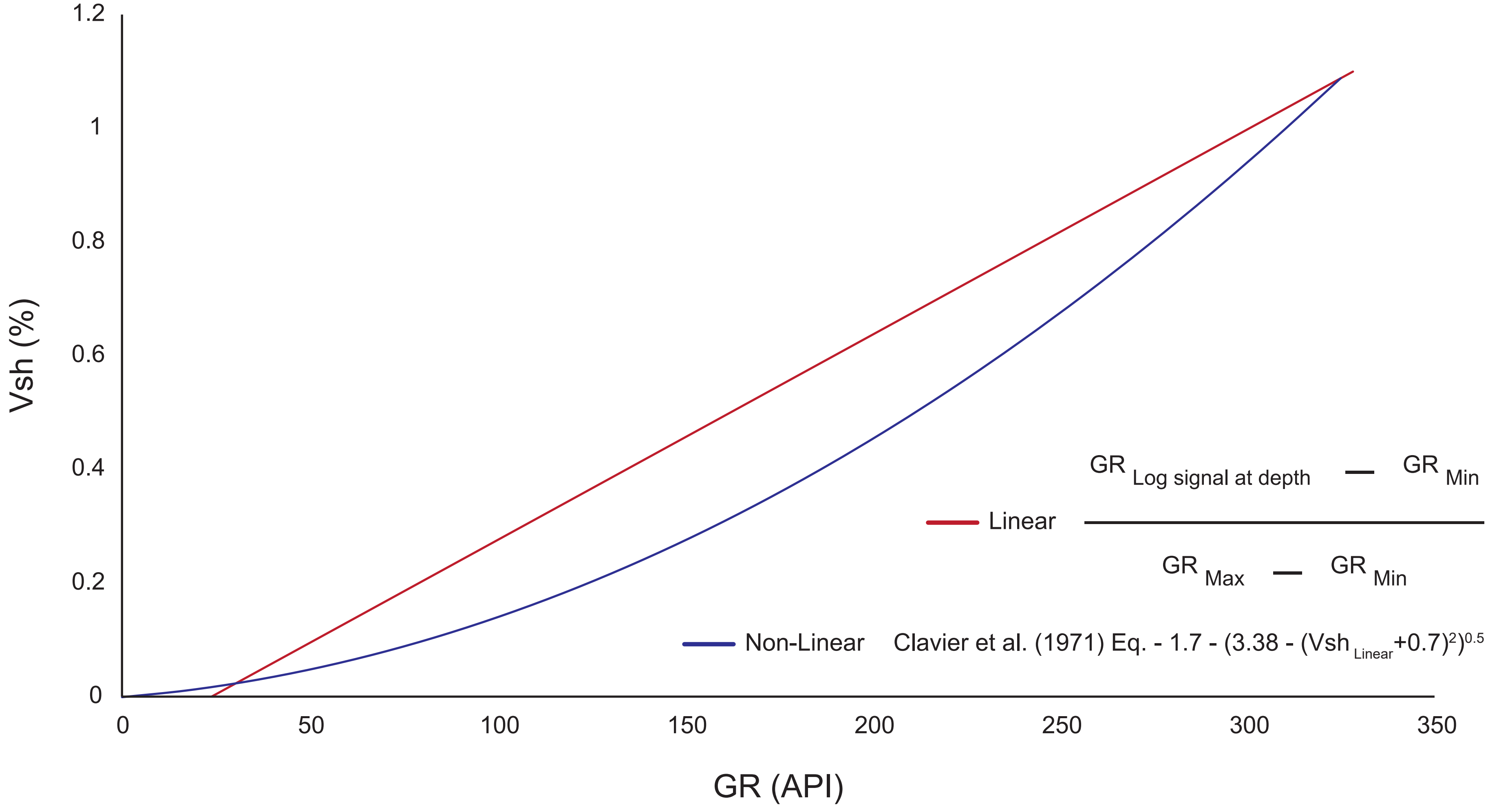

Appendix 9. Volume of shale (Vsh) estimations from Gamma Ray (GR) log responses.

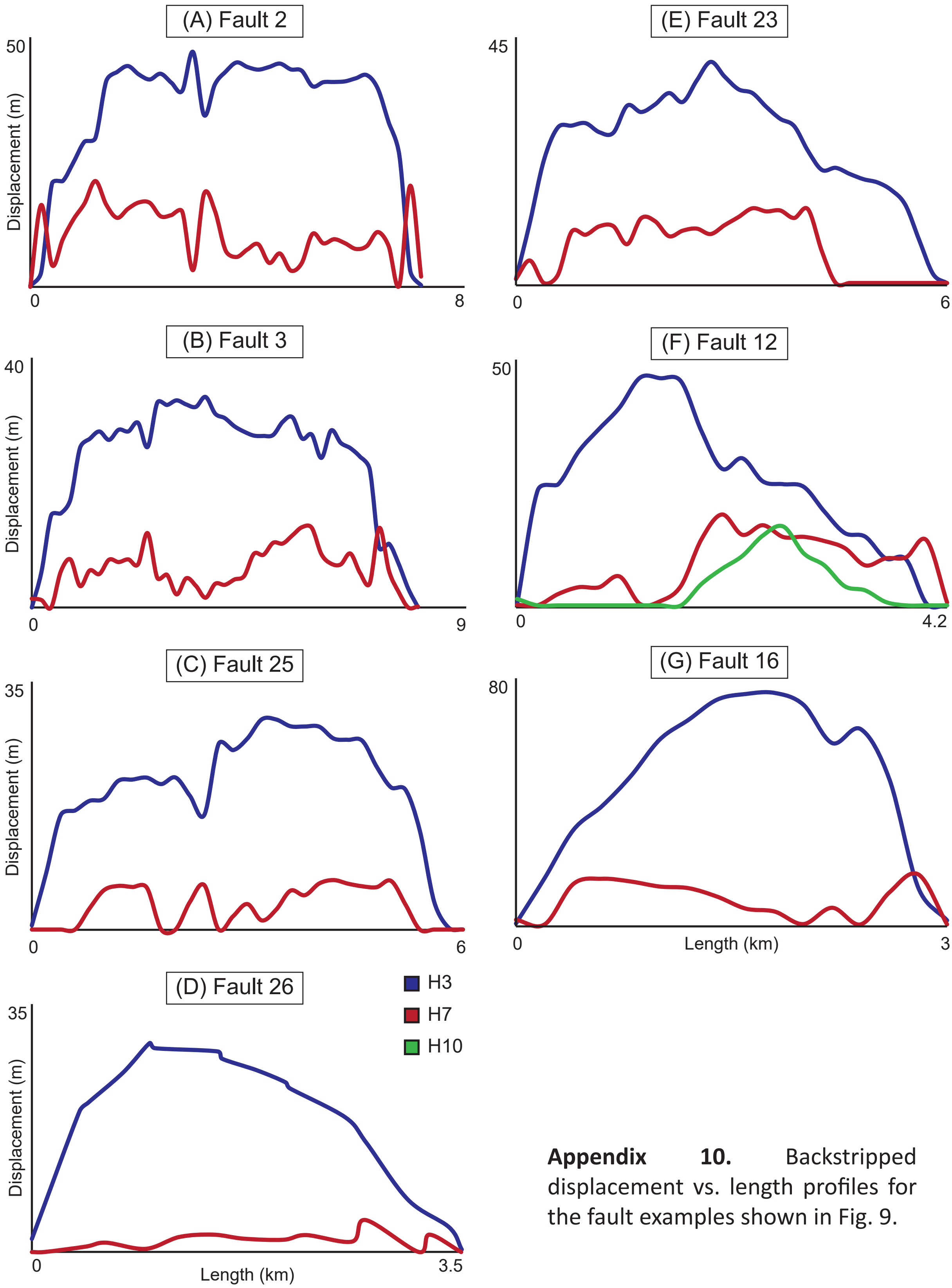

Appendix 10. Backstripped displacement vs. length profiles for the fault examples shown in Fig. 9.

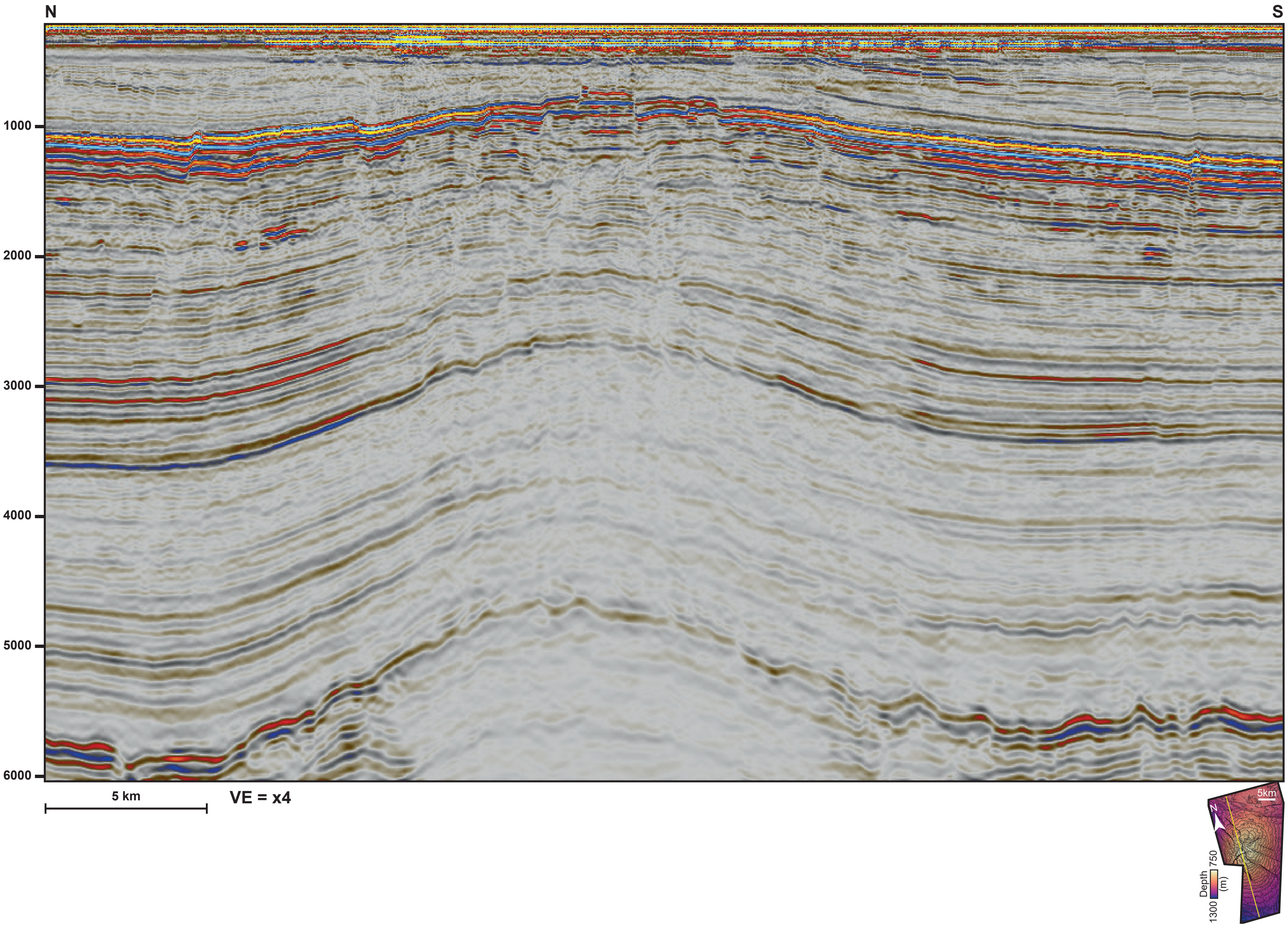
N
S
1000
2000
3000
4000
5000
6000
5 km
VE = x4
5km
N
Depth (m)
750
1300

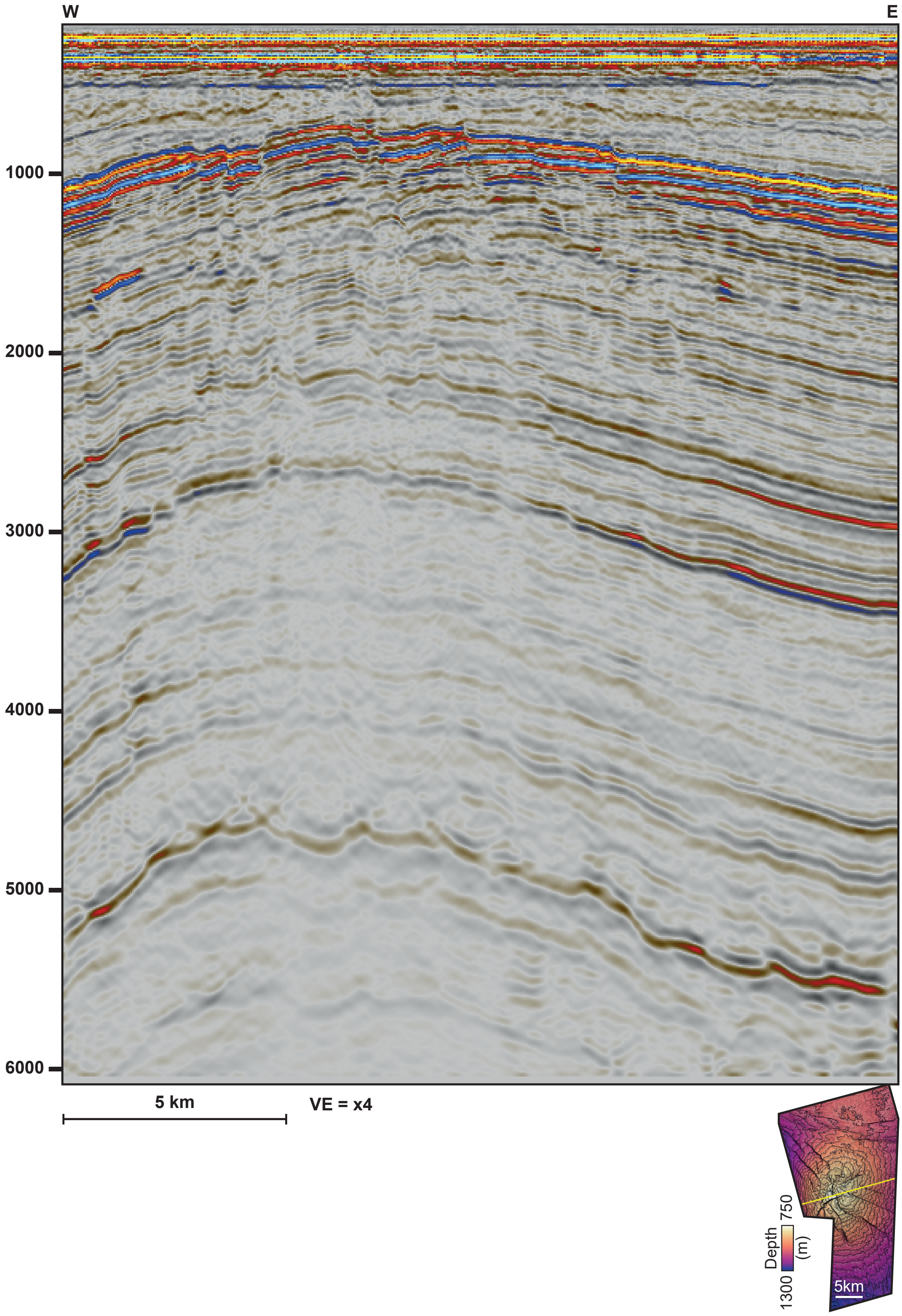

Appendix 11. IL and XL seismic lines crossing the Samson Dome that show the full depth coverage of the seismic survey used in Chapters 4 and 5.